Micro-Scale Control of Oligodendrocyte Morphology and Myelination by the Intellectual Disability-Linked Protein Acyltransferase ZDHHC9

Hey-Kyeong Jeong[1*], Estibaliz Gonzalez-Fernandez[1*], Ilan Crawley[1], Jinha Hwang[2], Dale D. O. Martin[1,3], Shernaz X Bamji[4], Jong-Il Kim[2], Shin H Kang[1,5†] and Gareth M Thomas[1,5†]

[1]Shriners Hospital Pediatric Research Center, Lewis Katz School of Medicine at Temple University, 3500 N Broad Street, Philadelphia, PA 19140, USA

[2]Department of Biomedical Science, Seoul National University College of Medicine, Seoul, Korea

[3]Current address: Department of Biology, University of Waterloo, Canada

[4]Department of Cellular and Physiological Sciences, Life Sciences Institute and Djavad Mowafaghian Centre for Brain Health, University of British Columbia, Canada

[5]Department of Neural Sciences, Lewis Katz School of Medicine at Temple University, 3500 N Broad Street, Philadelphia, PA 19140, USA

*Equal contribution

[†]Correspondence to gareth.thomas@temple.edu or shin.kang@temple.edu

Abstract

Mutations in the X-linked *ZDHHC9* gene cause cognitive deficits in humans, with a subset of patients suffering from epilepsy. X-linked intellectual disability (XLID) is often ascribed to neuronal deficits, but here we report that expression of human and mouse ZDHHC9 orthologs is far higher in myelinating oligodendrocytes (OLs) than in other CNS cell types. *ZDHHC9* codes for a protein acyltransferase (PAT), and we found that ZDHHC9 is the most highly expressed PAT in OLs. Wild type ZDHHC9 localizes to Golgi outposts in OL processes, but other PATs and XLID mutant forms of ZDHHC9 are restricted to OL cell bodies. Using genetic tools for OL progenitor fate tracing and sparse cell labeling, we show that mice lacking *Zdhhc9* have grossly normal OL development but display extensive morphological and structural myelin abnormalities. Consistent with the hypothesis that these deficits are OL-autonomous, they are broadly phenocopied by acute *Zdhhc9* knockdown in cultured conditions. Finally, we found that ZDHHC9 palmitoylates Myelin Basic Protein (MBP) in heterologous cells, and that palmitoylation of MBP is impaired in the *Zdhhc9* knockout brain. Our findings provide critical insights into the mechanisms of *ZDHHC9*-associated XLID and shed new light on the palmitoylation-dependent control of myelination.

Introduction

Mutations in the *ZDHHC9* gene cause X-linked Intellectual Disability (XLID)(1-3). XLID-associated *ZDHHC9* mutations include nonsense mutations and missense mutations affecting key amino acids, as well as splice site mutations, insertions, and deletions that result in frameshifts. Importantly, all these genetic changes are predicted to be loss-of-function. These findings suggest that ZDHHC9 is essential for higher brain function.

Given that many XLID genes are neuronally enriched (4-10), an *a priori* hypothesis is that ZDHHC9 acts in neurons. However, patients with *ZDHHC9* mutations have grossly normal gray matter (GM) but reduced brain white matter (WM) volume, especially in the corpus callosum (CC) (1-3). *ZDHHC9* mutations are also linked to cerebral palsy, a condition in which intellectually disability is often associated with WM impairment (WMI) (11-14). These findings raise the possibility that ZDHHC9 may be crucial for normal WM development and/or proper function of oligodendrocytes (OLs), the myelin-forming CNS glia abundant in WM. Notably, *Zdhhc9* knockout (KO) mice exhibit WM volume reductions and seizure-like activity (15, 16), as well as behavioral phenotypes seen in other mouse models of ID (15). Thus, *Zdhhc*9 KO mice have the potential to serve as an excellent model for human ZDHHC9 mutations. However, their phenotype is yet to be fully characterized.

ZDHHC9 codes for a protein acyltransferase (PAT), an enzyme that catalyzes the modification of protein cysteine residues with palmitate and related fatty acids. This process, termed palmitoylation (also known as *S*-palmitoylation or *S*-acylation), plays a critical role in targeting proteins to specific subcellular membrane locations (17). Nearly 30 years ago, it was reported that major myelin proteins in the nervous system, including Proteolipid protein (PLP), Myelin basic protein (MBP), Myelin-associated glycoprotein (MAG) and Myelin oligodendrocyte glycoprotein (MOG), are palmitoylated (18, 19). However, at that time, methods were lacking to define roles of palmitoylation of these proteins in myelin formation and function. Later proteomic studies revealed

many other palmitoylated myelin proteins (20-23), and an isolated study suggested that palmitoylation targets myelin proteins to the plasma membrane of cultured OLs (24). Despite these findings, little is known regarding how myelin protein palmitoylation is regulated and the functional importance of this process for higher brain function.

We hypothesized that ZDHHC9-dependent palmitoylation plays a critical role in proper myelination and WM formation. Consistent with this notion, we report that ZDHHC9 is the most highly expressed PAT in mouse and human OLs. Moreover, ZDHHC9 localizes to puncta in OL processes that are likely Golgi outposts, whereas other PATs tested and *ZDHHC9* XLID mutant forms are restricted to OL cell bodies. These findings may explain why *ZDHHC9* loss of function cannot be compensated by other PATs. In mice lacking *Zdhhc9*, we did not detect changes in OL lineage cell generation or total MBP expression levels, but we found that at the micro-scale *Zdhhc9* KO OLs are dysmorphic and myelin ultrastructure is highly abnormal, with both hypo- and hypermyelination of axons in WM tracts. We show that with the help of Golga7, a ZDHHC9 partner protein that also localizes to Golgi outposts, ZDHHC9 robustly palmitoylates the major myelin protein MBP, and that MBP palmitoylation is impaired in *Zdhhc9* KO brain. Palmitoyl- and total levels of another myelin protein, Myelin-associated Glycoprotein (MAG) are also affected by *Zdhhc9* KO, suggestive of a broader deficit in myelin protein regulation and organization in these mice. Together, our findings provide new insights into mechanisms of *ZDHHC9*-associated XLID and the palmitoylation-dependent control of myelination, a process first reported decades ago, but about which almost nothing is known.

Results

Cell-Specific Transcriptomics Reveals That ZDHHC9 and Its Partner Protein GOLGA7 Are Enriched in Oligodendrocytes in the Mouse and Human Brain

To assess *Zdhhc9* expression in OLs, we performed FACS using cerebral cortex (CTX) of P30 *Mobp-EGFP* BAC transgenic (Tg) mice, which express EGFP only in mature OLs (Fig. 1A; (25, 26)). We isolated RNA from the EGFP$^+$ OLs and performed OL-specific RNA sequencing (RNA-Seq). Total RNA was also extracted from the cortices of the same mice without OL sorting and used for a separate bulk RNA-Seq. Bioinformatics analysis indicated that genes previously known to be highly expressed in myelinating OLs (14) were highly enriched in our OL-specific RNA preparations (Fig 1B). In contrast, expression levels of genes specific to other neural cell types and endothelial cells were very low, confirming that our transcriptomic dataset is highly OL-specific (Fig. 1B).

We then extracted fragments per kilobase of transcript per million mapped reads (FPKM) values for all ZDHHC family PATs from our OL-specific RNA-Seq dataset. We found that *Zdhhc9* is the most highly expressed PAT in OLs (FPKM ~ 180), with mRNAs for *Zdhhc14*, *Zdhhc17*, and *Zdhhc20* present at lower but detectable levels (FPKM 30 ~ 70) (Fig.1C). The remaining PATs were expressed at far lower levels (FPKM <10). These results suggest that ZDHHC9 is the predominant PAT in myelinating OLs.

ZDHHC9 activity requires a conserved partner, Golgi Complex Protein-16 (gene name *Golga7*)(16, 27, 28). We found that *Golga7* was also abundantly expressed in OLs, at far higher levels than other Golga family members, including *Golga7*'s closest paralog, *Golga7b* (Fig. 1D). FPKM values for *Zdhhc9* and *Golga7* were far lower in total RNA preps obtained from whole cortices without specific cell type isolation (Fig. 1E, left Heatmap), suggesting that high *Zdhhc9* and *Golga7* expression is an OL-specific feature, rather than a general characteristic of CNS cells. Consistent with this notion, examination of another CNS cell type-specific RNA-Seq dataset, obtained with sorted cells from P17 brain cortices via immunopanning (29), confirmed high and

specific expression of *Zdhhc9* and *Golga7* in myelin-forming OLs (Fig. 1E, right Heatmap). Moreover, examination of a human RNA-Seq study (30) revealed that, like mouse CNS, both *ZDHHC9* and *GOLGA7* are enriched in human OLs, compared to any other PATs or other GOLGA family members, respectively. (Fig 1F). Together, these findings raise the possibility that ZDHHC9, in concert with GOLGA7, plays an important role in OLs.

Wild type ZDHHC9 and GOLGA7 Localize to Oligodendrocyte Processes *In Vitro,* Unlike Other PATs or ZDHHC9 Mutants

As a first step toward understanding ZDHHC9 function in OLs, we sought to define the subcellular localization of transfected HA-tagged ZDHHC9 (HA-ZDHHC9) in cultured OLs. We also compared the subcellular localization of HA-ZDHHC9 with that of HA-tagged forms of ZDHHC3, ZDHHC7 and ZDHHC17, three other ZDHHC-PATs that are implicated in nervous system regulation and which are expressed in OLs *in vivo* (Fig. 1E, (29, 31-36)).

After three days of culture in differentiation medium (Fig 2A), cultured OLs were extensively ramified and showed strong MBP immunofluorescence ('OL3D'; Fig S1A). We transfected these cultured OLs and fixed them 9h later to minimize the likelihood of ZDHHC-PAT expression itself altering OL morphology and affecting HA-PAT subcellular localization (Fig 2A). Under these conditions, HA-ZDHHC3, HA-ZDHHC7, and HA-ZDHHC17 were only detected in OL cell bodies, consistent with their restriction to the somatic Golgi in other cell types (32, 35, 37-39) (Fig 2B, D). In contrast, HA-ZDHHC9 was detected both in OL cell bodies and in discrete puncta in OL processes (Fig. 2B, D). Within OL cell bodies, ZDHHC9 partially colocalized with the Golgi marker GM130 (Fig. S1A, B). Consistent with this Golgi localization, ZDHHC9 also colocalized in part with additional Golgi markers (TGN38, Giantin; Fig S1C, D). However, these markers were not detected in OL processes and therefore did not colocalize with ZDHHC9 in this latter location (Fig. S1A-D).

We also compared the subcellular distribution of wild type ZDHHC9 (ZDHHC9WT) with that of XLID-associated ZDHHC9 mutants (R96W; R148W; P150S) (40, 41). In contrast to HA-ZDHHC9WT, these XLID-associated HA-ZDHHC9 mutants did not localize to OL processes (Fig. 2C, D). These results raise the possibility that dysregulated subcellular localization of ZDHHC9, rather than, or in addition to, reduced catalytic activity (42) is a causative factor in *ZDHHC9* loss of function mutations in XLID.

We also sought to define the localization in OLs of Golga7, which directly binds and enhances function of ZDHHC9 in other cell types (16, 27, 28). Consistent with this role, myc-tagged Golga7 (myc-Golga7) colocalized extensively with HA-ZDHHC9 in both OL cell bodies and in discrete puncta in OL processes (Fig. S2A). We then sought to further define the identity of these discrete ZDHHC9/Golga7-positive puncta. In neurons, specialized Golgi outposts and Golgi satellites can function as acentrosomal microtubule-organizing centers (MTOCs) in dendrites (43-47). Interestingly, Golgi outposts were also recently reported to be present in OLs (48), and a subset of OL Golgi outposts can be marked by the proteins TPPP and Mannosidase II (ManII) (45, 47, 48). Consistent with their assignation as Golgi outposts, ZDHHC9-positive puncta in OL processes colocalized with GFP-tagged ManII (ManII-GFP) and, to a lesser extent, with Flag-tagged TPPP (TPPP-Flag) (Fig. S2B, C).

The OL processes in this culture condition correspond to large lipid-rich membranous sheets that form spiral membrane expansion on axons *in vivo* (49). ZDHHC9's localization to Golgi outposts/satellites in processes of cultured OLs suggest its potential role in myelin formation (myelination) and/or maintenance. Moreover, this function of ZDHHC9 might not be shared with other PATs tested and may be impaired in XLID-associated mutant forms of ZDHHC9.

No detectable changes in Oligodendrocyte Development or Gross Myelination in *Zdhhc9* KO Mice

To address whether *Zdhhc9* regulates OL development and myelination *in vivo*, we examined the brains of *Zdhhc9* KO mice. Histological observations of brain sections from 6-week-old male mice revealed no apparent difference in MBP-labeled OL processes between WT control and *Zdhhc9* KO mice (Fig. 3A). OL numbers in CTX and the corpus callosum (CC), assessed using OL markers aspartoacylase (ASPA) or Quaking 7 (recognized by antibody CC1), also did not detect any significant difference between the two groups (Fig. S3A-C). To quantify OLs more precisely, we crossed *Zdhhc9* KO with *Mobp-EGFP* mice and counted EGFP-labeled OLs. Again, we did not detect significant differences in EGFP$^+$ OL density between the two genotypes in three examined CNS regions (CTX, CC, and spinal cord), at two different ages (P28, P56; (Fig. 3B, C)). We also detected no difference in the density of NG2$^+$ OL progenitor cells (OPCs) between WT and *Zdhhc9* KO mice (Fig. 3D, E).

We next asked whether *Zdhhc9* loss affects the rate of oligodendrogenesis (maturation of OPCs to OLs). To address this question, we crossed *Zdhhc9* KO mice with *Pdgfra-CreER; R26-EGFP* (RCE) mice (50) and analyzed the fates of genetically labeled OPCs. Control (*Pdgfra-CreER; RCE*) and KO (*Pdgfra-CreER; RCE*; *Zdhhc9*$^{y/-\text{ or }-/-}$) mice received tamoxifen injections at P21 and were sampled 3 weeks later (P21+21) (Fig. 3F-1). This allowed us to label PDGFRα$^+$ OPCs with EGFP at P21 and track their differentiation. Newly differentiated EGFP$^+$ OLs from the previously labeled EGFP-labeled OPCs were analyzed (Fig. 3F-2, G). However, we did not detect differences in the number of newly formed EGFP-labeled ASPA$^+$ OLs and % of EGFP$^+$ OLs (Fig. 3H, I) and the ratio of OLs to OPCs among EGFP-labeled cells (data not shown) between the two groups. These results suggest that *Zdhhc9* KO does not alter oligodendrogenesis in either the young or mature CNS, at least using the markers and methodologies that we employed.

Zdhhc9 KO Impairs Microstructure of Oligodendrocyte Processes

Although we did not detect differences in overall oligodendrogenesis or myelin production, we reasoned that loss of *Zdhhc9* might still affect the targeting of specific myelin proteins to the

membrane, resulting in irregular formation of processes in OLs or abnormalities in myelin. To address this possibility, we used a sparse genetic OL labeling method, crossing *Mobp-iCreER*; *mT/mG* mice to *Zdhhc9* KO mice. By P56, a small degree of tamoxifen-independent (leaky) Cre activity leads to spontaneous expression of membrane-anchored EGFP (mEGFP) in a subset (~5%) of cortical OLs in these mice. The sparsely EGFP-labeled brain sections were then imaged with confocal microscopy to detect mEGFP signal in CTX and to subsequently trace OL processes (Fig. 4A). The morphology of individual OLs was then reconstructed as a 3D skeleton (Fig. 4B). Sholl analysis of these reconstructions revealed that the overall OL process complexity was slightly increased in *Zdhhc9 KO* mice (Fig. 4C). More surprisingly, the primary and secondary branch process were longer in *Zdhhc9* KO than control mice (Fig. 4D).

We also analyzed the processes of individual OLs in raw images from these sections. In control mice, the EGFP-labeled processes originating from one OL soma were of similar thickness, with a uniformly smooth structure. However, the thickness of mEGFP$^+$ processes in *Zdhhc9* KO mice was far more heterogenous, with several spheroid-like swellings (Fig. 5A, B). The abnormal thickness of EGFP$^+$ OL processes may reflect dysregulated axon recognition by OLs. Notably, the abnormal spheroid-like swellings on OL processes were distinguished from OL somas as they lack signal for DAPI or Olig2 (Fig. 5C, Fig. S4). Careful tracing of EGFP$^+$ OL processes connected to DAPI$^+$ cell body and quantification of spheroid-like swellings devoid of DAPI signal (Fig. 5C-1, C-2) revealed significant structural abnormalities in OL processes in *Zdhhc9* KO mice (Fig. 5D, E). These results indicate that, in contrast to its lack of effect at the gross level, *Zdhhc9* loss greatly alters the structure of individual OL processes at the microscopic level, presumably due to abnormal OL membrane expansion.

Impaired Myelination in *Zdhhc9* KO Mice

The non-uniformity of *Zdhhc9* KO OL processes suggests that *Zdhhc9* loss may disrupt the typical bias of myelination based on axon caliber and/or the spreading of the OL membrane

along the axon. To address this issue, we examined the extent and pattern of axonal myelination using electron microscopy (EM) (Fig. 6A). In electron micrographs from P56 CC, the number of axons did not differ between WT and *Zdhhc9* KO mice (Fig. 6A, B). However, while most axons were evenly myelinated in WT mice, myelin patterns of axons in *Zdhhc9* KO mice were highly abnormal; with many large axons unmyelinated (Fig. 6A, C) and a subset of small diameter axons (< 0.5 μm) appearing to be hypermyelinated (Fig. 6A, D). Consistent with the latter finding, *g*-ratios of these small diameter axons were smaller in *Zdhhc9* KO mice (Fig. 6E, F).

Next, we inquired whether the dysmyelination observed in young adult (P56) *Zdhhc9* KO mice resulted from impaired initial myelination or from impaired myelin maintenance or active demyelination. At P30, a time at which myelination is actively ongoing, EM images showed a broadly similar extent of myelination across all axons in WT mice (Fig. 6G, H). However, in *Zdhhc9* KO mice, both hypo- and hypermyelination of axons was already noticeable at this developmental stage (Fig. 6G), which was evident from an increased interquartile range of *g*-ratios (Fig. 6H, I). These findings suggest that *Zdhhc9* loss results in dysmyelination and, thus, that ZDHHC9 is required for proper initial myelination of individual axons.

Evidence supporting a cell-autonomous role of ZDHHC9 in Oligodendrocyte Maturation

Zdhhc9 is constitutively deleted in the KO mice, so OL morphological abnormalities and myelination deficits seen in this line might be caused by loss of action of ZDHHC9 in other cell types. As a first step to testing whether phenotypes in *Zdhhc9* KO mice are cell-autonomous, we delivered lentivirus expressing GFP plus a specific shRNA (16) to knock down *Zdhhc9* in WT OPCs in culture and induced OPC-to-OL differentiation one day later (Fig. 7A). *Zdhhc9* knockdown OLs had significantly reduced expression of MBP, compared to OLs infected to express a scrambled shRNA (Fig. 7B-D).

We asked whether this failure to express and distribute MBP is due to impaired commitment to the OL lineage in culture. However, *Zdhhc9* knockdown OLs still expressed 2',3'-

Cyclic nucleotide 3'-phosphodiesterase (CNP), an early myelin-specific protein of developing OLs (51) (Fig. S5). This result suggests that ZDHHC9 is not required for initial differentiation of OPCs to OLs, consistent with the normal number of OLs seen in *Zdhhc9* KO mice *in vivo* (Fig. 3C, Fig. S3C). However, consistent with the reduced and restricted MBP expression, *Zdhhc9* knockdown OLs were also morphologically immature (Fig. 7E) with a reduced degree of branching confirmed by Sholl analysis (Fig. 7F). These data indicate that *Zdhhc9* loss cell-autonomously impairs OL maturation *in vitro*.

A ZDHHC9-Golga7 PAT Complex Directly Palmitoylates MBP

Finally, we sought to identify potential ZDHHC9 substrates in OLs. Myelination of CNS axons by OLs requires the targeting of myelin proteins, including MBP, PLP, MOG and MAG, to the myelin membrane. These myelin proteins are all palmitoylated (20, 24, 52-54), but the PAT(s) that controls myelin protein palmitoylation was not previously identified. We thus used a non-radioactive palmitoylation assay, acyl biotin exchange (ABE) (55, 56), to determine whether ZDHHC9 can directly palmitoylate MBP in co-transfected HEK293T cells. Palmitoylation of 21.5 kDa MBP (one of two MBP isoforms that contains a cysteine residue and is thus capable of undergoing palmitoylation) was very low when transfected alone. MBP palmitoylation remained very low when either HA-ZDHHC9 or myc-Golga7 were co-transfected in isolation (Fig. 8A, B). However, MBP palmitoylation was greatly increased by co-transfection of HA-ZDHHC9 and myc-Golga7 (Fig. 8A, B).

Finally, we asked if ZDHHC9 likely palmitoylates MBP *in vivo*. We used ABE to purify palmitoyl-proteins from forebrain WM tissue (CC and striatum) of WT and *Zdhhc9* KO mouse brains. Consistent with *in vivo* immunostaining results (Fig. 3A), *Zdhhc9* KO did not affect total MBP levels measured by western blotting (all isoforms assessed together; Fig 8C, D). Two MBP bands were detected in ABE (palmitoyl) fractions, which based on their molecular weights, likely represent the 17.0 and 21.5 kDa isoforms of MBP (57). Like 21.5 kDa MBP, the 17.0 kDa form of

MBP contains a cysteine residue and may be subject to palmitoylation (57). Importantly, palmitoylation, but not total expression, of both the 17 kDa and 21.5 kDa MBP isoforms was significantly reduced in *Zdhhc9* KO mice (Fig. 8C, D). Total and palmitoyl- levels of MAG were also significantly reduced in *Zdhhc9* KO mice, although the palmitoyl:total ratio of MAG was not. In the same samples, neither palmitoyl-, total, nor palmitoyl:total levels of Cadm4 were affected in *Zdhhc9* KO mice. This latter finding is consistent with a report ascribing Cadm4 palmitoylation to a different PAT (58). Together, these results suggest that ZDHHC9 directly palmitoylates MBP with the support of Golga7 and that *Zdhhc9* loss impairs MBP palmitoylation. In addition, *Zdhhc9* loss impacts other myelin protein levels and/or regulation.

Discussion

Genetic factors are central to intellectual disability (59, 60), as exemplified by the increasing number of known XLID-associated genes (61-64). However, knowledge of the cellular/molecular processes controlled by XLID-associated gene products is often limited. The cognitive deficits and epilepsy that are hallmarks of *ZDHHC9*-associated XLID are often ascribed to malformations of neocortical gray matter (65-69). Indeed, ZDHHC9 is expressed in a subset of forebrain neurons (70), and '*Zdhhc9* knockdown' primary hippocampal neurons display impaired dendritic branching and an altered ratio of excitatory-to-inhibitory synapses (16). However, there is an increasing appreciation that ID can also result from impaired WM formation and/or function (71-75). Consistent with this notion, both ZDHHC9 and its partner protein Golga7 are far more highly expressed in OLs than in other CNS cell types, in both mice and humans (Fig. 1E, F, (29, 31)). In support of a key role for ZDHHC9 in normal WM formation and function, we found that *Zdhhc9* KO does not affect axon number in the CC, but greatly impacts microscale OL morphology and myelin ultrastructure (Figs. 4 - 6). We recognize that using conventional *Zdhhc9* KO mice, in which *Zdhhc9* is globally deleted, cannot directly address whether impaired myelination in these mice is due to a cell-autonomous role for ZDHHC9 in OLs, a role for ZDHHC9 in neurons, or a combination of these factors. However, the impaired OL morphology and maturation seen in culture conditions after acute *Zdhhc9* loss (Fig. 7) supports the first of these possibilities. While a conditional KO mouse could more directly help test the OL-autonomous role of ZDHHC9 in vivo, in this study we focused on conventional KO mice to more accurately mirror the situation in human patients with *ZDHHC9* loss or mutation.

It is perhaps surprising that, despite the clear changes in OL morphogenesis, we did not detect changes in overall numbers of OPCs or OLs in *Zdhhc9* KO mice. However, we cannot exclude the possibility that such changes could be revealed by different methods. In addition, different OL subtypes express different subsets of other marker genes (75) and it remains possible that *Zdhhc9* loss preferentially directs OL maturation towards or away from one or more

of these subtypes. Furthermore, we cannot exclude the possibility that assessment of other brain regions might also reveal differences in OPC and/or OL numbers in *Zdhhc9* KO mice. Lastly, we also note that acute *Zdhhc9* loss in cultured OLs causes more striking phenotypes than seen with KO mice *in vivo*. However, it is not uncommon for acute knockdown to cause more dramatic effects than germline KO, possibly due to longer-term compensatory mechanisms *in vivo* (76, 77). Together, though, our findings suggest that OL and WM abnormalities could significantly contribute to *ZDHHC9*-associated XLID.

Based on behavioral milestones, patients with *ZDHHC9*-associated XLID have been diagnosed as young as two years of age (41), suggesting that ZDHHC9 is important for higher brain function during early development. Consistent with this notion, we observed dysmyelination (both hyper and hypomyelination) in P30 mice, approximately equivalent to a 3-year-old human (78). These findings suggest that the myelin abnormalities observed in adult *Zdhhc9* KO mice (Fig. 6) are due to impaired myelination, rather than impaired myelin maintenance, and further support the use of *Zdhhc9* KO mice as a model for human *ZDHHC9*-associated XLID.

Zdhhc9 is also expressed at higher levels than other PATs in OLs (Fig 1C, E, F), potentially explaining much of the impact of *Zdhhc9* loss in these cells. However, it is also intriguing that ZDHHC9 localization in OLs differs markedly from that of other PATs examined (Fig 2). Moreover, ZDHHC9 and Golga7 colocalize as discrete puncta in cultured OL processes, and our immunostaining results with subcellular organelle markers suggest that these puncta represent Golgi outposts or satellites (Fig. 2, Fig. S2)(47, 48). Of the PATs we tested, none were targeted to these locations, providing a possible additional, and non-mutually exclusive, reason why *Zdhhc9* loss cannot be readily compensated for in OLs.

Golgi outposts have long been known in neurons (79), and we previously reported that ZDHHC9 localizes to such structures in primary hippocampal neurons (16). Golgi outposts were also recently described in OLs, where their function remains to be fully determined (46). Thus, the role(s) of ZDHHC9 at this subcellular organelle in OLs is challenging to infer. Nonetheless,

we speculate that ZDHHC9 could be involved in either or both of the best-described roles of Golgi outposts, protein glycosylation and microtubule nucleation, for the following reasons. First, ZDHHC9-positive Golgi outposts in OL processes are also positive for the enzyme Mannosidase II, suggesting they represent sites at which protein glycosylation is regulated (Fig. S2B). In addition, although ZDHHC9 colocalization with TPPP, a protein implicated in microtubule nucleation, is less apparent (Fig. S2C), knockout/knockdown of either ZDHHC9 (Figs. 4 and 7) or TPPP (48) affects branching and complexity of OL processes, a process that involves microtubule nucleation. However, more investigation is needed to determine the functions of Golgi outposts in OLs, in order to define the associated contribution of ZDHHC9.

Another intriguing question is whether and how the loss of ZDHHC9 action at Golgi outposts might contribute to the myelination deficits we observed in *Zdhhc9* KO mice (Figs. 5 and 6). Our sparse genetic labeling studies revealed that *Zdhhc9* KO OL processes are distended, with numerous spheroid-like swellings (Fig. 5). It appears very possible that the hypo- and hypermyelination of *Zdhhc9* KO axons seen in single-plane EM cross-sections (Fig. 6) represents this same distension phenotype, observed using a different method. Although beyond our current technical abilities, we speculate that EM-based reconstruction in 3 dimensions would reveal regions of both hypo- and hypermyelination of individual callosal axons in *Zdhhc9* KO mice.

How, though, might *Zdhhc9* loss cause dysmyelination? Several myelin proteins are palmitoylated, and we found that a ZDHHC9/Golga7 complex palmitoylates the major myelin protein MBP and that MBP palmitoylation is reduced in forebrain WM of *Zdhhc9* KO mice (Fig. 8). Given that palmitoylation can sort proteins to the myelin membrane (24), the simplest explanation might be that impaired palmitoylation of MBP, and potentially other myelin proteins, in the absence of ZDHHC9 affects myelin structure per se. We also observed slight but significant reductions in palmitoyl- and total levels of MAG in the absence of ZDHHC9 (Fig S6A, B), which may also contribute to impaired myelination. In contrast, ZDHHC9 loss did not alter palmitoyl- or total levels of Cadm4, a myelin protein whose palmitoylation is ascribed to the Golgi-localized PAT ZDHHC3

(58)(Fig S6C, D). These latter finding suggests that, although ZDHHC9 loss may affect additional myelin proteins, gross, widespread dysregulation of myelin protein levels and/or palmitoylation in the absence of ZDHHC9 is unlikely. An important additional factor to consider, however, is that ZDHHC9 substrates also include other proteins that act at Golgi outposts to direct myelin proteins to the correct region of the myelin membrane and/or to ensure uniform distribution of myelin proteins within that membrane. A comparison of WT and *Zdhhc9* KO palmitoyl-proteomes could help determine which of these possibilities (which are not mutually exclusive) best accounts for impaired myelination in the absence of ZDHHC9.

In summary, we reveal an unexpectedly non-heterogeneous expression of *Zdhhc9* in both mice and humans, with biased expression in mature OLs. Moreover, within OLs, WT ZDHHC9 localizes uniquely compared to other PATs examined, and to XLID-associated forms of ZDHHC9. Although we did not detect changes in overall OL numbers or gross myelin staining, we found that *Zdhhc9* loss greatly impairs OL morphology and myelination at the microscale. These findings provide new insights into mechanisms of *ZDHHC9*-associated XLID and into other conditions marked by WMI.

Materials and Methods

Mice

Zdhhc9 knockout mice (B6;129S5-Zdhhc9tm1Lex/Mmucdm) were originally obtained from Mutant Mouse Resource and Research Center (MMRRC), UC Davis and were previously described (16). Mice were transferred from University of British Columbia to Temple University School of Medicine for this study. Female heterozygous *Zdhhc9* knockout mice were bred with male wildtype C57BL/6 mice to obtain male *Zdhhc9* hemizygous knockout and male wild-type mice as littermate controls, which were used for experiments in Figures 6 and 8. Experiments in Figs. 3 - 5 used a mixture of male *Zdhhc9* hemizygous KO (*Zdhhc9* $^{y/-}$) and female *Zdhhc9* homozygous KO (*Zdhhc9* $^{-/-}$) mice. *Mobp-EGFP* BAC Tg (26) (generated by GENSAT; MMRRC stock #030483-UCD, RRID:MMRRC_030483-UCD), *R26-CAG-LSL-EGFP (RCE)* (80) (MMRRC stock #032037-JAX, RRID:MMRRC_032037-JAX) and *Mobp-iCreER* mice (80) were described previously and obtained from Dr. Dwight Bergles (Johns Hopkins University). *Pdgfra-CreER*^{TM} BAC Tg ((81); RRID:IMSR_JAX:018280) and mT/mG mice (82) were purchased from the Jackson Laboratory. Mice were housed in a barrier facility with a 12h:12h light: dark cycle, were provided food and water *ad libitum* and were checked daily by ULAR staff. All procedures involving vertebrate animals followed National Institutes of Health guidelines and were approved by the Institutional Animal Care and Use Committee (IACUC) of Temple University.

Fluorescence-activated cell sorting (FACS)

After the whole brain was isolated from one-month-old *Mobp-EGFP* mice, one hemisphere of the forebrain was chopped with a blade into small pieces. The brain cells were further dissociated using a Neural Dissociation Kit (Miltenyi Biotec) according to the manufacturer's instruction. After enzymatic digestion, the cells were mechanically dissociated with gentle pipetting and suspended in Hank's Balanced Salt Solution (GIBCO). The cell suspension was passed through a 40-μm cell strainer (Corning). Cells were re-suspended in 0.5% FBS in HBSS and isolated with BD influx

(BD Biosciences) at the Flow Core Facility of Temple University School of Medicine. The other hemisphere of each mouse brain was used for total RNA isolation.

RNA Sequencing

Total RNAs were extracted from the FACS-isolated EGFP$^+$ OLs with RNeasy Micro kit (Qiagen). For total RNA extraction from the other hemisphere forebrain (without OL sorting), we homogenized the brains with Trizol reagent (Invitrogen). All RNA samples were subjected to Quality Control with Bioanalyzer (Agilent), and the RNA samples whose RIN was higher than 8 were used for subsequent applications. Ten ng of total RNA was used in the Ovation RNA-Seq System v2 (NuGEN) to prepare cDNA library. Following manufacturer's instructions, total RNA and primer were incubated at 65 °C for 5 min, followed by first-strand cDNA synthesis (4 °C for 1 min, 25 °C for 10 min, 42 °C for 10 min, 70 °C for 15 min, and then cooling to 4 °C) and second strand cDNA synthesis (4 °C for 1 min, 25 °C for 10 min, 50 °C for 30 min, 80 °C for 20 min and then cooling to 4 °C). RNAClean XP bead purification was performed. Single Primer Isothermal Amplification (SPIA) was used to amplify cDNAs. QIAquick cleanups (Qiagen) were eluted in 30 µl low EDTA TE buffer and quantified via Nanodrop 1000. 100 ng amplified SPIA cDNA was sonicated using a Covaris E210 (50 µl, duty cycle 10%, intensity 5, 200 burst/sec, 45 sec) to shear samples to 350bp. The libraries were prepared using the TruSeq DNA LT Sample Prep Kit (Illumina) according to manufacturer's instructions. Samples were purified using sample purification beads. End repair reaction (at 30 °C for 30 min) was followed by bead purification and size selection for 350bp insert. dA-tailing (37 °C for 30 min, 70 °C for 5 min, 4 °C for 5 min) and adapter ligation with barcoded adapters were performed (30 °C for 10 min), followed by bead purification and PCR amplification (95 °C for 3 min; 8 cycles of 98 °C for 20 sec, 60 °C for 15 sec and 72 °C for 30 sec; 72 °C for 5 min). A final bead purification was performed, and libraries were quantified using the Agilent Bioanalyzer High Sensitivity DNA assay. For the forebrain total RNA library (all cell RNA-seq), 500 ng of RNA was used for library generation

with TruSeq Stranded mRNA Library Prep Kit (Illumina). Sequencing was performed using an Illumina HiSeq 2000.

RNA-Seq Data Analyses

RNA-seq reads were aligned to a mouse reference genome (mm10) by the STAR alignment tool (v2.4.0) with default option and PCR duplicate reads were removed using the Picard Tools (v1.124). To quantify expression levels for each gene, we counted the number of aligned fragments for each gene using HTSeq-0.6.1 with parameters (-s no, -r pos, -f bam, -m intersection-nonempty and -t exon) according to the Ensembl mouse transcript annotation (GRCm38.74 version) and calculated the FPKM (Fragments Per Kilobase per Million mapped reads) values of each gene. For heatmap visualization, the FPKM values for each gene were color-coded with the Microsoft Excel color scales.

Accession Codes

The RNA-seq files have been uploaded to the European Nucleotide Archive (ENA) under accession code PRJEB19341.

Tamoxifen Administration

Cre activity was induced with tamoxifen (Sigma-Aldrich, Cat# T5648) administration to *Pdgfra-CreER* mice. Tamoxifen was dissolved (20 mg/ml) in a mixture of sunflower seed oil-ethanol (10:1), and then ethanol was evaporated in a vacuum concentrator for 30 min. Forty mg/kg (b.w.) of tamoxifen was intraperitoneally (i.p.) injected twice daily with at least a 6 hour interval between injections. A total of 8 doses of tamoxifen was injected into the *Pdgfra-CreER mice; RCE;* ± *Zdhhc9 KO* mice between P21 and P24.

Rat Primary OPC Culture and Differentiation

Primary mixed glial cultures were prepared from P1 rat pups, as previously described (83). Briefly, cortices were isolated and digested with papain and DNase I, followed by mechanical dissociation. Cells were resuspended in DMEM supplemented with 10% (v/v) fetal bovine serum and 1% (w/v) penicillin/streptomycin. Cells were plated in T75 flasks coated with poly-D-lysine and medium was replaced every other day. Under these conditions, a mixed population of glial cells survives and proliferates, but neuronal cells do not survive. After 7~10 days, these mixed glial cultures were shaken overnight (14~16 hours). Detached cells were added to uncoated petri dishes, to which microglia preferentially adhere but OPCs do not. The OPC-enriched supernatant was then plated on poly-D-lysine coated coverslips. OPCs were maintained in defined OPC media containing PDGF (10 ng/ml) and bFGF (5 ng/ml). The following day, fresh OPC medium was added, and the medium was refreshed every other day. To induce OPC differentiation, OPC medium was replaced by defined OL medium containing triiodothyronine (T3, 30 ng/ml and T4, 40 ng/ml), CNTF (10 ng/ml) and NT3 (1 ng/ml).

Molecular Biology

Wildtype mouse *Zdhhc3*, *Zdhhc7*, *Zdhhc9* and *Zdhhc17* cDNAs (all with N-terminal HA tag) were a kind gift from Dr. Masaki Fukata (National Institute of Physiological Sciences, Okazaki, Japan) and were subcloned into lentiviral expression vector (FEW) downstream of the EF1α promoter and an N-terminal HA tag, as described (37). XLID mutant forms of *Zdhhc9* (human point mutations introduced into mouse cDNA) were generated as *BsrGI* – *AfeI* gBlock fragments (Integrated DNA Technologies) and were used to replace the wildtype *Zdhhc9 BsrGI* – *AfeI* fragment *via* standard subcloning. Mouse *Golga7* and MBP (21.5kDa isoform) cDNAs were synthesized as *XhoI-NotI* gBlock fragments and subcloned into a modified FEW vector downstream of an N-terminal myc epitope tag. Mouse *Tppp* cDNA was synthesized (Genewiz) and subcloned into modified FEW vector upstream of a C-terminal Flag tag. C-terminally GFP-tagged Mannosidase cDNA was obtained from Addgene (plasmid #160905) and used without

additional subcloning. Membrane-bound GFP (mGFP) cDNA was generated by appending the N-terminal 40 amino acids of MARCKs to eGFP (84) as a *PspXI – HindIII* fragment, which was then subcloned into FEW vector with no additional tag.

Lentiviral Vectors and Lentivirus Preparation

VSV-G pseudotyped lentiviruses were prepared as described (56), except that viruses were collected in DMEM containing 0.1% (v/v) FBS and were added to cultured cells without ultracentrifugation.

Lentiviral Infection and OL Differentiation

For *Zdhhc9* knockdown, OPCs were infected at two days *in vitro* (DIV2) with lentiviral vectors carrying *Zdhhc9* shRNA or a control scrambled shRNA (16). OPC media was refreshed at 4 hours and one day post-infection, and then the medium was replaced with defined OL medium at one day post-infection for differentiation. The OL culture medium was then refreshed every other day. Infected OLs were fixed at 9 DIV ('OL 6 days') for immunostaining.

Transfection of Cultured OPCs

To define the subcellular localization of ZDHHC PATs and other proteins in OLs, differentiated OLs at 6 DIV ('OL 3 days') were transfected with plasmids using Lipofectamine LTX with Plus Reagent (Thermo Fisher Scientific) according to the manufacturer's recommendations. Briefly, plasmid DNA (diluted in Opti-MEM, GIBCO, Thermo Fisher Scientific, Waltham, MA) was mixed with 1.5ul of PLUS™ Reagent and incubated for 5 min at room temperature (RT). 1ul of Lipofectamine® LTX (diluted in opti-MEM) was added to pre-incubated DNA and incubated for 30 min at RT for generation of DNA-lipid complex. This DNA-lipid complex was applied to the cells for transfection, and OLs were fixed 9 hours later and processed for immunostaining.

Immunocytochemistry (ICC)

Coverslips containing OL cells were rinsed with 1x Recording buffer (25mM HEPES pH7.4, 120mM NaCl, 5mM KCl, 2mM $CaCl_2$, 1mM $MgCl_2$, 30mM Glucose) and cells were fixed for 20 min in PBS containing 4% paraformaldehyde (PFA)/ 4% sucrose. Coverslips were washed 3X 10 min in phosphate buffered saline (PBS) and blocked for 1 hr at room temperature with 10% (v/v) normal goat serum (NGS; Thermo Fisher Scientific, Waltham, MA) in PBST containing 0.15% Triton X-100. Cells were then incubated in blocking solution with primary antibodies overnight at 4°C, washed 3X 10 min in PBS, incubated in secondary antibodies in blocking solution for 1 hour at RT, washed 3X 10 min in PBS, and mounted on microscope slides using FluorSave reagent (Millipore Sigma). Confocal images were captured with a laser scanning confocal microscope (Leica TCS SP8) and LAS X software.

Quantification of ICC images

To quantify distribution of HA-tagged PATs in OL processes (Fig. 2), confocal images of HA (PAT) and GFP (cell fill) signal were thresholded. The same threshold values for each channel were used across all images. Using the Sync Windows tool in ImageJ/Fiji, the cell body area was traced in the GFP channel image and deleted from both images. Both images were then inverted and the ADD function was used to generate an image of the HA+/GFP+ signal. Using the Analyze particles tool (with settings 0-infinity pixels sq and 0.00-1.00 circularity), the combined area occupied by the HA+/GFP+ puncta was calculated and normalized to the total extra-somatic GFP+ area from the GFP+ image of the same cell.

The percentage of GFP^+/MBP^+ cells (Fig. 7B) was counted manually without thresholding, using the same criteria for all conditions. Sholl analysis in Fig 7E, F was performed by manually reconstructing the morphology of individual OLs in ImageJ/Fiji as a binarized image. OL nuclei were considered the center, and concentric circles were drawn with an interval of 10 μm and the number of intersections calculated using the ImageJ/Fiji Sholl Analysis plug-in.

The percentage of morphologically immature OLs (Fig. S5) was calculated manually based on identification of GFP^+/CNP^+ cells (committed OLs) that did not show the 'pancake'-like morphology of mature OLs and plotted as a percentage of all GFP^+/CNP^+ cells per field. Morphologically immature OLs also typically lacked MBP staining (as in Fig 7B) but this property was not used in the Fig S5 analysis.

Immunofluorescence of Brain Sections

Mice were anesthetized with pentobarbital sodium (70 mg/kg, i.p) and transcardially perfused with PBS followed by 4% PFA. Mouse brains were post-fixed overnight at 4˚C and transferred to 30 % sucrose in PBS at 4˚C. Brain tissues were frozen in Tissue-Tek optimum cutting temperature (O.C.T.) compound (Sakura, Cat# 4586) and sectioned using a Leica Biosystems CM1950 Cryostat. Three different thicknesses of brain or spinal cord sections were used: 20 μm for MOBP-EGFP-based or ASPA-staining dependent OL quantification, 35 μm for OPC fate analysis, and 50 μm for mEGFP-based OL morphological analysis. Brain and spinal cord sections were stained in a free-floating manner. Sections were permeabilized with 0.3% (w/v) Triton X-100 and blocked with blocking solution (5% (v/v) normal donkey serum, 0.3% (w/v) Triton X-100) for 1 hour at RT. Sections were then incubated in blocking solution containing primary antibodies at 4˚C overnight. On the next day, sections were rinsed with PBS 3X 5 min and incubated with secondary antibodies and DAPI (1:1,000) in blocking solution at RT for 2 hours. Sections were rinsed in PBS 3X 5 min and then mounted onto slide glasses with a mounting medium with ProLong antifade (Thermo Fisher Scientific, P36970). Image acquisition of the immunostained brain sections was performed with a wide-field fluorescent microscope AxioImager M2 (Zeiss) or a laser scanning confocal microscope TCS SP8 (Leica).

Morphological Analysis of Oligodendrocytes

The settings for OL tracing were kept the same for all the samples across genotypes. Confocal images were captured for sparsely labeled randomly chosen EGFP$^+$ OLs from the CTX (layers IV–VI). Images of labelled cells were imported into Fiji and traced without z-projecting the stacks. Sholl analysis was performed using Fiji plug-in. For Sholl analysis of OLs in vivo, the OL nuclei were considered the center, and concentric circles were drawn with an interval of 5 μm. Imaris 9.9 (Oxford Instrument) software was used for 3D surface rendering of OLs with representative confocal images.

Electron Microscopy and *g*-ratio Analysis

Mice were anesthetized with pentobarbital sodium (100 mg/kg, i.p) and transcardially perfused with PBS followed by 2.5% PFA, 2% glutaraldehyde (in 0.1 M phosphate buffer, pH 7.4). Mouse brains were post-fixed overnight at 4˚C and transferred to 0.1 M phosphate buffer at 4˚C. Brains were dehydrated using a graded ethanol series and embedded into Embed-812 (EMS). Thin sections were prepared, stained with uranyl acetate and lead citrate and visualized with an electron microscope (JEOL 1010 electron microscope fitted with a Hamamatsu digital camera) at the University of Pennsylvania Electron Microscopy Resource Laboratory. 15,000X magnified images and Fiji Plug-in and ImageJ/Fiji (85) were used for the g-ratio analysis of myelin. To analyze potentially hypermyelinated small axons in P56 mice, g-ratio was calculated using the ratio of inner-to-outer diameter (distance values derived from pixel intensity along plot profile generated in ImageJ/Fiji) of each myelinated axon. To analyze myelination of all axons in P30 mice, inner and outer diameters of axons were traced manually in ImageJ/Fiji and the resultant diameters calculated.

Acyl Biotinyl Exchange Assay

HEK cells were transfected using a calcium phosphate-based method as described (56). Cells were lysed 8h post-transfection and ABE assays performed as in (56). For WM tissue collection from *Zdhhc9* knockout and littermate control mice, mice were anesthetized with pentobarbital sodium (100 mg/kg, i.p). Brains were isolated and briefly rinsed with ice-cold HBSS buffer (no calcium, no magnesium). Using a Mouse Brain Slicer, 1mm block coronal brain sections were prepared on ice and WM-enriched tissues including corpus callosum and striatum were dissected from slices under a dissection microscope. Dissected WM tissue was homogenized in a glass-teflon dounce homogenizer (20 strokes, 200 rpm) in 4mM HEPES, 0.32M sucrose, containing freshly diluted Protease Inhibitor Cocktail (PIC; Roche). Homogenized samples were transferred to a fresh tube, rapidly brought to room temperature, and solubilized by addition of 1/10 volume of 10% (w/v) SDS. Samples were centrifuged for 10 minutes at 4˚C at 13,000 rpm to pellet insoluble material and protein concentrations in supernatants determined by BCA assay (Pierce). Protein concentrations were normalized by addition of homogenization buffer containing SDS and PIC and were used for ABE assay as described (56).

Quantification and Statistical Analysis

All data were analyzed using GraphPad Prism software (GraphPad Software, San Diego, CA). In all graphs the mean is shown, and error bars indicate standard error of the mean (SEM). For the quantitative comparisons of OL lineage cells, OPC fate analysis, and OL process complexity, two-way ANOVA and Šidák's multiple comparison test were used. For spheroid structure comparison, unpaired student's t-test was used.

Antibodies

The following antibodies, from the indicated sources, were used for ICC

Anti-HA-Tag (Rb IgG), Cell Signaling technology #3724 (C29F4), 1:100

anti-HA.11 Epitope Tag (mouse IgG1), Covance HA.11 #MMS-101P, 1:100

GFP (Rb IgG), Invitrogen #A11122, 1:1000

GFP (mouse IgG2a), Invitrogen #A11120 (3E6), 1:500

Myc (mouse IgG1), Cell signaling #92013(E7F9B), 1:200

MBP (chicken IgG), Aves Lab #MBP, 1:1000

CNP (Rb IgG), Phosphosolutions #325-CNP, 1:1000

Secondary antibodies for ICC were Alexa Fluor 488-, 568- or 647-conjugated goat IgG against mouse IgG1 or IgG2a, rabbit or chicken (Thermofisher Scientific, 1:500).

The following antibodies, from the indicated sources, were used for Immunofluorescence

anti-APC (mouse IgG2b) EMD Millipore #OP80 (CC1), 1:50

anti-ASPA (Rb IgG) GeneTex #GTX113389, 1:500

anti-GFP (goat IgG) Rockland, #600-101-215, 1:500

anti-MBP (Rb IgG) Cell Signaling Technology #78896 (D8X4Q), 1:500

anti-NG2 (guinea pig IgG) gift from Dr. Bergles, Johns Hopkins University, 1:4000

Olig2 (goat IgG) R&D #AF2418, 1:500.

Secondary antibodies for immunofluorescence were Alexa Fluor 488-, Cy3-, Cy5-, or Alexa Fluor 647-conjugated donkey IgG against goat, rabbit, or guinea pig (Jackson ImmunoResearch, 1:500).

The following primary antibodies, from the indicated sources, were used for western blotting:

anti-HA.11 Epitope Tag (mouse IgG1), Covance HA.11 #MMS-101P, 1:5000

anti-MAG (Rb IgG) Cell Signaling Technology #9043, 1:500

anti-MBP (Rb IgG) Cell Signaling Technology #78896 (D8X4Q), 1:500

anti-Myc (rabbit) Cell Signaling Technology #2278 (71D10), 1:500

anti-Cadm4 / SynCAM4 (mouse) Antibodies Inc.#75-247 1:100

Acknowledgements

We thank P. Kanuparthi, L. Hernandez, N. Hesketh and S. Yungblut (all Thomas lab) for help with molecular biology, EM image acquisition, ABE assays and *g*-ratio quantification, respectively. We also gratefully acknowledge Dr. M Fukata for PAT cDNAs and Dr. D Bergles for *Mobp-iCreER* mice and anti-NG2 antibody. Supported by grants from NINDS (R21 NS125202-01 to G.M.T; R01 NS089586 to S.H.K.), Ellison Medical Foundation (AG-NS-1101-13 to S.H.K), and Shriners' Childrens (87400PHI to G.M.T).

Figure Legends:

Figure 1: Oligodendrocyte-specific transcriptomics reveals OL-enriched expression of ZDHHC9 and GOLGA7. ***A:*** Fluorescent image of widespread EGFP expression in the brain of *Mobp-EGFP* mice (Left). Confocal images of EGFP and other cell-specific markers (NG2 for OPC, CC1 for OLs, and NeuN for neurons) (Right). White arrowheads indicate colocalization of $EGFP^+$ cells and CC1-immunoreactivities. Boxed area in left panel corresponds to the region used to acquire confocal images for NG2 and CC1 in right panel. Scale bars: 500 (left) and 20 (right) μm. ***B:*** Heatmap for expression levels of previously reported cell type-specific gene clusters from the OL-specific RNA-Seq results. $EGFP^+$ OLs were isolated from cortices of three *Mobp-EGFP* mice with FACS, and their RNAs were used for RNA-Seq. ***C, D:*** FPKM values of ZDHHC-protein acyltransferases (PATs) (C) and Golgin subfamily A members (D) expressed in OLs. ***E:*** Heatmap of relative expression of all PATs and Golgin subfamily A member genes in mouse OLs and other brain cells according to data from this study (left) and *Zhang et al., 2014* (Ref. #28; right). ***F:*** Heatmap of relative expression of all PATs and Golgin subfamily A member genes in human OLs and other brain cells according to *Zhang et al., 2016* (Ref. #29).

Figure 2: HA-ZDHHC9WT localizes to puncta in OL processes, but other PATs, and XLID mutant forms of ZDHHC9, are restricted to OL cell bodies. ***A:*** Experimental timeline. ***B:*** Images of morphologically mature OLs transfected as in *A* to express the indicated HA-tagged PATs and immunostained with the indicated antibodies. Lower panels show enlarged images of the boxed regions in upper panels. ***C:*** Images as in lower panels of *B* of OLs transfected to express WT HA-ZDHHC9 or the indicated XLID mutant forms of ZDHHC9. ***D:*** Quantified data confirms that HA-ZDHHC9 WT occupies a greater percentage of the total OL area (GFP+ area) compared with other PATs, or with HA-ZDHHC9 XLID mutants. *: p=0.032 (HA-ZDHHC9WT vs HA-ZDHHC3); p=0.0053 (HA-ZDHHC9WT vs HA-ZDHHC7); p=0.004 (HA-ZDHHC9WT vs HA-ZDHHC17); p=0.0036 (HA-ZDHHC9WT vs HA-ZDHHC9-R96W); p=0.0058 (HA-ZDHHC9WT vs

HA-ZDHHC9-P150S); p=0.0047 (HA-ZDHHC9WT vs HA-ZDHHC9-R148W), Data are from 3-5 cells per condition, pooled from n=3 cultures.

Figure 3: No detectable gross abnormality in oligodendrocyte development in *Zdhhc9* KO mice. ***A:*** Fluorescent (upper) and confocal (bottom) images of MBP immunostaining in the brain of 6-week-old WT and *Zdhhc9* KO mice. MBP confocal images were taken from layers IV/V of CTX. Scale bars: 500 (upper panel) and 20 (bottom) µm. ***B:*** Fluorescent (upper) and confocal (bottom) images of EGFP in the brain of 8-week-old control (*Mobp-EGFP*) and *Zdhhc9* KO (*Mobp-EGFP; ZDHHC9*$^{y/-}$) male mice. EGFP confocal images were taken from the CC. Scale bars: 500 (upper panel) and 50 (bottom) µm. ***C:*** Quantification of EGFP^{+} OLs in CTX, CC, and spinal cord (SC) from 4-week (P28) and 8-week (P56)-old control and *Zdhhc9* KO *Mobp-EGFP* mice (n=3 – 5 mice for each group). Two-way ANOVA and pair-wise comparison was performed with Šidák's multiple comparison test. ns: not significant. ***D:*** Confocal images of cortical NG2^{+} OPCs in 8-week-old WT and *Zdhhc9* KO male mice. Scale bar: 50 µm. ***E:*** Quantification of the density of NG2^{+} OPCs in CTX of 4-week-old WT and *Zdhhc9* KO mice (n=3 per group). Unpaired Student's t-test. ***F-1:*** Experimental scheme for OPC fate tracing. *Pdgfra-CreER; RCE* and *Pdgfra-CreER; RCE; Zdhhc9* KO mice were administered with tamoxifen injection starting at P21 for 3 days, and mouse brains were sampled at P42. ***F-2:*** Schematic diagram of OPC fate tracing. ***G:*** Confocal images of EGFP, NG2, and ASPA in CTX of control and Zdhhc9 KO *Pdgfra-CreER; RCE* mice (P21+21). *Yellow arrowheads*: overlapping signals between EGFP and NG2; *white arrows*: overlapped signals between EGFP and ASPA. Scale bars: 50 µm. ***H:*** Quantification of EGFP^{+}NG2^{+} OPCs and EGFP^{+}ASPA^{+} OLs. ***I:*** Percentage of NG2^{+} OPCs and ASPA^{+} OLs among EGFP^{+} cells. Data are mean ± SEM (E, H, I). For H and I, N= 10 (control) or 7 (*Zdhhc9* KO) male and female mice. Two-way ANOVA and pair-wise comparisons were performed with Šidák's multiple comparison tests. ns: not significant.

Figure 4: Genetic sparse cell labeling reveals altered complexity of oligodendrocyte processes in *Zdhhc9* KO mice. *A:* Experimental flow of the sparse genetic labeling of OLs, from acquisition of confocal images of mEGFP from CTX in P56 *Mobp-iCreER; mT/mG* mice to 3D OL process tracing to Sholl analysis. mEGFP signal allows for detailed process morphology of individual OLs, compared to more complex 'bulk' MBP signal. ***B:*** Representative results from tracing of OL processes. Scale bars: 20 µm. ***C, D:*** Branch numbers (C) and process length (D) were compared between control (*Mobp-iCreER; mT/mG*) and Zdhhc9 KO (*Mobp-iCreER; mT/mG; Zdhhc9 KO*) mice. N=15 OLs (5 OLs per mouse, three mice per group). Two-way ANOVA and pair-wise comparisons were performed with Šidák's multiple comparison tests (C and D). ns: not significant. *, $p < 0.05$; **, $p < 0.01$.

Figure 5: Abnormal oligodendrocyte processes in *Zdhhc9* KO mice. *A:* Confocal microscopy of mEGFP in P56 *Mobp-iCreER; mT/mG* mice reveals morphological abnormalities, such as non-homogenous $EGFP^+$ cell processes and spheroid-like membrane folding (yellow arrowheads). Scale bar: 20 µm. ***B:*** 3D-reconstruction of $EGFP^+$ OLs and $DAPI^+$ nuclei from the images shown in (A) with the Imaris software. Scale bar: 7 µm. ***C:*** OL processes and connected OL cell body were traced. Two different cells are shown in magenta and green. Arrowheads indicate spheroid-like swelling. ***D, E***: Quantification of process abnormalities per field (D) and per cell (E). N=15 cells from 3 mice per group. Student's t-test. ***, $p < 0.001$.

Figure 6: Altered myelination in *Zdhhc9* KO corpus callosum *in vivo*. *A:* Electron micrographs of corpus callosum axons from P56 male mice of the indicated genotypes. Wild type axons are uniformly myelinated, but in *Zdhhc9* KO some large axons are hypomyelinated (red dotted outline), while a subset of small axons appear hypermyelinated (blue dotted outline). There

is also frequent dysmyelination (green asterisk). ***B:*** Quantification of images from *A* reveal no change in total number of axons in *Zdhhc9* KO. n.s.: not significant (p=0.7117, t test, N=3 mice per genotype). ***C:*** Percentage of unmyelinated axons from mice of the indicated genotypes (N=3 mice per genotype; *;p=0.0036, t test). ***D:*** number of hypermyelinated small axons per field in corpus callosum images from mice of the indicated genotypes (N=3 mice per genotype; *; p=0.0150, t test). ***E:*** G-ratio of small diameter axons (0.1-0.5 μm) from mice of the indicated genotypes. ***F:*** Average G-ratio from *E* confirms hypermyelination of small diameter axons in P50 *Zdhhc9* KO mice. ***G:*** as *A*, but from P30 mice. Deficits in myelination are already evident at this time. ***H:*** As *E*, but for all axons from *G.* ***I:*** Increased heterogeneity of myelination in *Zdhhc9* KO corpus callosum at P30, represented by an increased interquartile range of G-ratios (*;p=0.0425, t test).

Figure 7: ZDHHC9 loss cell-autonomously impairs maturation of cultured OLs. ***A:*** Timeline of experiment. ***B:*** Immunofluorescent images of cultured OLs, after infection with the indicated lentiviruses and fixation as in *A.* ***C:*** Quantified data from *B* reveal that *Zdhhc9* knockdown reduces the percentage of GFP-expressing (virally infected) MBP^+ cells i.e., mature OLs (**; p=0.0067, t-test, n=4 individual cultures per condition). ***D:*** Likewise, *Zdhhc9* knockdown reduces the percentage of MBP-expressing GFP+ cells. (*; p=0.0359, t-test, n=4 individual cultures per condition). ***E:*** *Left:* Images of individual OLs after infection and fixation as in *B. Middle column:* reconstructed outline of individual OLs. *Right column:* Images from middle column with superimposed concentric circles for Sholl analysis. ***F:*** Sholl analysis from OLs reconstructed as in *E* confirms reduced morphological complexity of *Zdhhc9* knockdown OLs. n=8 cells per condition. *:p<0.05; **:p<0.01; ***:p<0.001; ****:p<0.0001, individual t tests.

Figure 8: ZDHHC9 palmitoylates MBP in cultured cells and *in vivo*. *A:* Western blots of palmitoyl- and total proteins from HEK293T cells transfected to express the indicated cDNAs. ***B:*** Quantified data from C confirms that co-transfection of HA-ZDHHC9 and myc-Golga7 greatly increase MBP palmitoylation. No signal for palmitoyl-MBP is seen in the absence of the key reagent hydroxylamine (NH_2OH), confirming assay specificity. **:$p<0.01$, Kruskal-Wallis test, n=5-6 experiments per condition. ***C:*** Western blots to detect MBP in total lysates and ABE fractions from forebrain WM (CC and striatum) from mice of the indicated genotype. ***D:*** Quantified data from *C* confirms that *Zdhhc9* loss reduces palmitoyl, but not total, levels of 17 kDa and 21.5 kDa MBP isoforms. palmitoyl:total 17.5 kDa isoform , n=15-16 per genotype; **:$p=0.0078$, palmitoyl:total 21 kDa isoform, n=8 per genotype,. 'N' number is lower for 21.5kDa MBP because in a subset of experiments this isoform was not efficiently extracted and was hence undetectable.

Supplementary Figure Legends

Figure S1: In OL cell bodies, ZDHHC9 localizes to somatic Golgi. ***A:*** *Left:* Experimental timeline for OL transfection experiments (duplicated from Fig 2A). *Center, right:* Images (maximum intensity projection of confocal z-slices) of cultured OLs after 3 days' incubation in differentiation medium ('OL3D'). Note extensively ramified morphology and MBP positivity, both of which are even more apparent after 6 days' differentiation ('OL6D'). ***B:*** Images of cultured OL (maximum intensity projection of confocal z-slices) transfected to express mGFP and HA-ZDHHC9 (timeline as in Fig 2A) and immunostained as indicated. ***C:*** Images of individual z-slices (planes 1-4) of the cell from *A* confirms colocalization of HA-ZDHHC9WT with Golgi marker GM130. ***D:*** Representative image of OL transfected to express HA-ZDHHC9WT (HA-9) and immunostained to detect HA, MBP and Golgi marker TGN38. ***E:*** As *D*, but for OL immunostained to detect HA, MBP and Golgi marker Giantin.

Figure S2: ZDHHC9-positive puncta in OL processes are Golgi outposts/satellites. ***A:*** Representative image of mature OL, transfected with the indicated cDNAs (timeline as in Fig.7A) and immunostained with the indicated antibodies. HA-ZDHHC9 WT colocalizes extensively with Golga7-myc in puncta in OL processes (arrows in zoomed images). ***B:*** As *A*, but for OLs transfected to express HA-ZDHHC9 WT, Golgi outpost marker ManII-GFP and mCherry. HA-ZDHHC9 colocalizes extensively with ManII-GFP in OL processes (arrows). ***C:*** As *A*, but for OLs transfected to express HA-ZDHHC9 WT, Golgi outpost marker TPPP-Flag and mGFP. HA-ZDHHC9 WT also colocalizes with TPPP-Flag in OL processes (arrows).

Figure S3: No alteration of oligodendrocyte density in *Zdhhc9* KO mice. ***A:*** Fluorescent images of ASPA$^+$ OLs in WT and *Zdhhc9* KO mice. ***B:*** Confocal images of ASPA, CC1, and Olig2

in the CTX and CC. Scale bars: 500 (A) and 25 (B) µm. ***C:*** Quantification of ASPA$^+$ OL densities. Data are mean ± SEM. Student's t-test. ns: not significant. P56 WT (n=4) and *Zdhhc9* KO (n=3) male mice.

Figure S4: Spheroid-like abnormal structures are distinct from Olig2$^+$ oligodendrocyte soma in *Zdhhc9* KO mice. Representative stacked confocal images of EGFP$^+$ OLs and Olig2 in control (A-1) and *Zdhhc9* KO (B-1) mice. Orthogonal views of the confocal images shown in A-1 (A-2) or in B-1 (B-2, B-3, and B-4). Scale bars: 20 µm. Asterisks denote Olig2$^+$ OL soma. Yellow arrowheads indicate abnormal swellings.

Figure S5: *Zdhhc9* knockdown causes morphological immaturity of committed OLs: *A:* Images of cultured OLs immunostained with the indicated antibodies. ***B:*** Quantified data from *A* confirm that *Zdhhc9* knockdown increases the percentage of immature (CNP$^+$, MBP$^-$) virally infected OLs, n=15 fields of view per condition from 2 coverslips per condition, from a single culture.

Figure S6: *Zdhhc9* loss impacts the palmitoyl-protein MAG but not Cadm4. *A:* Western blots to detect MAG in total lysates and ABE fractions from forebrain WM (CC and striatum) from mice of the indicated genotype. ***B:*** Quantified data from *A* confirm that *Zdhhc9* loss significantly reduces palmitoyl and total levels of MAG, but palmitoyl:total level is not significantly affected. ***C:*** As *A*, but blotted to detect Cadm4. ***D:*** Quantified data from *C* confirm that *Zdhhc9* loss does not significantly affect palmitoyl-, total or palmitoyl:total levels of Cadm4. *:$p<0.05$, n.s.; not significant, unpaired t-test, N=12 per genotype.

References

1. K. Baker *et al.*, Epilepsy, cognitive deficits and neuroanatomy in males with ZDHHC9 mutations. *Ann Clin Transl Neur* **2**, 559-569 (2015).
2. F. L. Raymond *et al.*, Mutations in ZDHHC9, which encodes a palmitoyltransferase of NRAS and HRAS, cause X-linked mental retardation associated with a Marfanoid habitus. *Am J Hum Genet* **80**, 982-987 (2007).
3. A. Masurel-Paulet *et al.*, Expanding the clinical phenotype of patients with a ZDHHC9 mutation. *Am J Med Genet A* **164A**, 789-795 (2014).
4. D. Devys, Y. Lutz, N. Rouyer, J. P. Bellocq, J. L. Mandel, The FMR-1 protein is cytoplasmic, most abundant in neurons and appears normal in carriers of a fragile X premutation. *Nat Genet* **4**, 335-340 (1993).
5. E. C. Budreck, P. Scheiffele, Neuroligin-3 is a neuronal adhesion protein at GABAergic and glutamatergic synapses. *Eur J Neurosci* **26**, 1738-1748 (2007).
6. A. Toya *et al.*, The distribution of neuroligin4, an autism-related postsynaptic molecule, in the human brain. *Mol Brain* **16**, 20 (2023).
7. L. Rusconi *et al.*, CDKL5 expression is modulated during neuronal development and its subcellular distribution is tightly regulated by the C-terminal tail. *J Biol Chem* **283**, 30101-30111 (2008).
8. F. C. Guarnieri *et al.*, A novel SYN1 missense mutation in non-syndromic X-linked intellectual disability affects synaptic vesicle life cycle, clustering and mobility. *Hum Mol Genet* **26**, 4699-4714 (2017).
9. J. A. Murphy, O. N. Jensen, R. S. Walikonis, BRAG1, a Sec7 domain-containing protein, is a component of the postsynaptic density of excitatory synapses. *Brain Res* **1120**, 35-45 (2006).
10. T. Bienvenu *et al.*, ARX, a novel Prd-class-homeobox gene highly expressed in the telencephalon, is mutated in X-linked mental retardation. *Hum Mol Genet* **11**, 981-991 (2002).
11. H. Jiang *et al.*, Early Diagnosis of Spastic Cerebral Palsy in Infants with Periventricular White Matter Injury Using Diffusion Tensor Imaging. *AJNR Am J Neuroradiol* **40**, 162-168 (2019).
12. E. Odding, M. E. Roebroeck, H. J. Stam, The epidemiology of cerebral palsy: incidence, impairments and risk factors. *Disabil Rehabil* **28**, 183-191 (2006).
13. C. L. van Eyk *et al.*, Targeted resequencing identifies genes with recurrent variation in cerebral palsy. *NPJ Genom Med* **4**, 27 (2019).
14. G. McMichael *et al.*, Whole-exome sequencing points to considerable genetic heterogeneity of cerebral palsy. *Mol Psychiatry* **20**, 176-182 (2015).
15. M. Kouskou *et al.*, Disruption of the Zdhhc9 intellectual disability gene leads to behavioural abnormalities in a mouse model. *Exp Neurol* **308**, 35-46 (2018).
16. J. J. Shimell *et al.*, The X-Linked Intellectual Disability Gene Zdhhc9 Is Essential for Dendrite Outgrowth and Inhibitory Synapse Formation. *Cell Rep* **29**, 2422-2437 e2428 (2019).
17. M. E. Linder, R. J. Deschenes, Palmitoylation: policing protein stability and traffic. *Nat Rev Mol Cell Biol* **8**, 74-84 (2007).
18. O. A. Bizzozero, L. K. Good, Myelin proteolipid protein contains thioester-linked fatty acids. *J Neurochem* **55**, 1986-1992 (1990).
19. H. C. Agrawal, R. E. Schmidt, D. Agrawal, In vivo incorporation of [3H]palmitic acid into PO protein, the major intrinsic protein of rat sciatic nerve myelin. *J Biol Chem* **258**, 6556-6560 (1983).
20. R. Kang *et al.*, Neural palmitoyl-proteomics reveals dynamic synaptic palmitoylation. *Nature* **456**, 904-909 (2008).

21. J. Wan *et al.*, Tracking brain palmitoylation change: predominance of glial change in a mouse model of Huntington's disease. *Chem Biol* **20**, 1421-1434 (2013).
22. E. L. Gorenberg *et al.*, Identification of substrates of palmitoyl protein thioesterase 1 highlights roles of depalmitoylation in disulfide bond formation and synaptic function. *PLoS Biol* **20**, e3001590 (2022).
23. M. J. Edmonds, B. Geary, M. K. Doherty, A. Morgan, Analysis of the brain palmitoyl-proteome using both acyl-biotin exchange and acyl-resin-assisted capture methods. *Sci Rep* **7**, 3299 (2017).
24. A. Schneider *et al.*, Palmitoylation is a sorting determinant for transport to the myelin membrane. *J Cell Sci* **118**, 2415-2423 (2005).
25. S. Gong *et al.*, A gene expression atlas of the central nervous system based on bacterial artificial chromosomes. *Nature* **425**, 917-925 (2003).
26. S. H. Kang *et al.*, Degeneration and impaired regeneration of gray matter oligodendrocytes in amyotrophic lateral sclerosis. *Nat Neurosci* **16**, 571-579 (2013).
27. J. T. Swarthout *et al.*, DHHC9 and GCP16 constitute a human protein fatty acyltransferase with specificity for H- and N-Ras. *J Biol Chem* **280**, 31141-31148 (2005).
28. P. L. Nguyen, W. K. Greentree, T. Kawate, M. E. Linder, GCP16 stabilizes the DHHC9 subfamily of protein acyltransferases through a conserved C-terminal cysteine motif. *Front Physiol* **14**, 1167094 (2023).
29. Y. Zhang *et al.*, An RNA-sequencing transcriptome and splicing database of glia, neurons, and vascular cells of the cerebral cortex. *J Neurosci* **34**, 11929-11947 (2014).
30. Y. Zhang *et al.*, Purification and Characterization of Progenitor and Mature Human Astrocytes Reveals Transcriptional and Functional Differences with Mouse. *Neuron* **89**, 37-53 (2016).
31. A. Zeisel *et al.*, Molecular Architecture of the Mouse Nervous System. *Cell* **174**, 999-1014 e1022 (2018).
32. C. Fang *et al.*, GODZ-mediated palmitoylation of GABA(A) receptors is required for normal assembly and function of GABAergic inhibitory synapses. *J Neurosci* **26**, 12758-12768 (2006).
33. J. Noritake *et al.*, Mobile DHHC palmitoylating enzyme mediates activity-sensitive synaptic targeting of PSD-95. *J Cell Biol* **186**, 147-160 (2009).
34. S. S. Sanders *et al.*, Sudden death due to paralysis and synaptic and behavioral deficits when Hip14/Zdhhc17 is deleted in adult mice. *BMC Biol* **14**, 108 (2016).
35. J. Niu *et al.*, Coupled control of distal axon integrity and somal responses to axonal damage by the palmitoyl acyltransferase ZDHHC17. *Cell Rep* **33**, 108365 (2020).
36. N. Kerkenberg *et al.*, Brain microstructural changes in mice persist in adulthood and are modulated by the palmitoyl acyltransferase ZDHHC7. *Eur J Neurosci* **54**, 5951-5967 (2021).
37. K. M. Collura *et al.*, The palmitoyl acyltransferases ZDHHC5 and ZDHHC8 are uniquely present in DRG axons and control retrograde signaling via the Gp130/JAK/STAT3 pathway. *J Biol Chem* **295**, 15427-15437 (2020).
38. Y. Ohno, A. Kihara, T. Sano, Y. Igarashi, Intracellular localization and tissue-specific distribution of human and yeast DHHC cysteine-rich domain-containing proteins. *Biochim Biophys Acta* **1761**, 474-483 (2006).
39. J. Greaves, C. Salaun, Y. Fukata, M. Fukata, L. H. Chamberlain, Palmitoylation and membrane interactions of the neuroprotective chaperone cysteine-string protein. *J Biol Chem* **283**, 25014-25026 (2008).
40. J. Y. Han *et al.*, The first patient with sporadic X-linked intellectual disability with de novo ZDHHC9 mutation identified by targeted next-generation sequencing. *Eur J Med Genet* **60**, 499-503 (2017).

41. S. Schirwani, E. Wakeling, K. Smith, M. Balasubramanian, Expanding the molecular basis and phenotypic spectrum of ZDHHC9-associated X-linked intellectual disability. *Am J Med Genet A* **176**, 1238-1244 (2018).
42. D. A. Mitchell *et al.*, Mutations in the X-linked intellectual disability gene, zDHHC9, alter autopalmitoylation activity by distinct mechanisms. *J Biol Chem* **289**, 18582-18592 (2014).
43. K. M. Ori-McKenney, L. Y. Jan, Y. N. Jan, Golgi outposts shape dendrite morphology by functioning as sites of acentrosomal microtubule nucleation in neurons. *Neuron* **76**, 921-930 (2012).
44. J. I. Valenzuela, F. Perez, Diversifying the secretory routes in neurons. *Front Neurosci* **9**, 358 (2015).
45. M. Mikhaylova, S. Bera, O. Kobler, R. Frischknecht, M. R. Kreutz, A Dendritic Golgi Satellite between ERGIC and Retromer. *Cell Rep* **14**, 189-199 (2016).
46. J. Wang, L. Fourriere, P. A. Gleeson, Local Secretory Trafficking Pathways in Neurons and the Role of Dendritic Golgi Outposts in Different Cell Models. *Front Mol Neurosci* **13**, 597391 (2020).
47. A. P. Govind *et al.*, Activity-dependent Golgi satellite formation in dendrites reshapes the neuronal surface glycoproteome. *Elife* **10** (2021).
48. M. M. Fu *et al.*, The Golgi Outpost Protein TPPP Nucleates Microtubules and Is Critical for Myelination. *Cell* **179**, 132-146 e114 (2019).
49. D. Fitzner *et al.*, Myelin basic protein-dependent plasma membrane reorganization in the formation of myelin. *Embo J* **25**, 5037-5048 (2006).
50. L. DeFlitch, E. Gonzalez-Fernandez, I. Crawley, S. H. Kang, Age and Alzheimer's Disease-Related Oligodendrocyte Changes in Hippocampal Subregions. *Front Cell Neurosci* **16**, 847097 (2022).
51. N. Baumann, D. Pham-Dinh, Biology of oligodendrocyte and myelin in the mammalian central nervous system. *Physiol Rev* **81**, 871-927 (2001).
52. J. M. Greer, B. Denis, R. A. Sobel, E. Trifilieff, Thiopalmitoylation of myelin proteolipid protein epitopes enhances immunogenicity and encephalitogenicity. *J Immunol* **166**, 6907-6913 (2001).
53. A. L. Pinner, J. Tucholski, V. Haroutunian, R. E. McCullumsmith, J. H. Meador-Woodruff, Decreased protein S-palmitoylation in dorsolateral prefrontal cortex in schizophrenia. *Schizophr Res* 10.1016/j.schres.2016.01.054 (2016).
54. M. Blanc *et al.*, SwissPalm: Protein Palmitoylation database. *F1000Res* **4**, 261 (2015).
55. J. Wan, A. F. Roth, A. O. Bailey, N. G. Davis, Palmitoylated proteins: purification and identification. *Nat Protoc* **2**, 1573-1584 (2007).
56. G. M. Thomas, T. Hayashi, S. L. Chiu, C. M. Chen, R. L. Huganir, Palmitoylation by DHHC5/8 targets GRIP1 to dendritic endosomes to regulate AMPA-R trafficking. *Neuron* **73**, 482-496 (2012).
57. K. Akiyama, S. Ichinose, A. Omori, Y. Sakurai, H. Asou, Study of expression of myelin basic proteins (MBPs) in developing rat brain using a novel antibody reacting with four major isoforms of MBP. *J Neurosci Res* **68**, 19-28 (2002).
58. J. Z. Yanli Chang, Chenchen Nie, Yajuan Lu, Fangjing Ren, Xize Cao, Juanjuan Li, Changhong Wang, Chenyu Yang, Tianhan Li, Yinming Liang, Shiqian Qi, Xiaohong Kang, Eryan Kong, DHHC3 mediated Cadm4 palmitoylation regulates myelination in CNS. *bioRxiv[Preprint] September 23, 2022. Available from https://doi.org/10.1101/2022.09.23.509146* (2022).
59. J. A. Vorstman, R. A. Ophoff, Genetic causes of developmental disorders. *Curr Opin Neurol* **26**, 128-136 (2013).
60. L. E. Vissers, C. Gilissen, J. A. Veltman, Genetic studies in intellectual disability and related disorders. *Nat Rev Genet* **17**, 9-18 (2016).
61. H. Renpenning, J. W. Gerrard, W. A. Zaleski, T. Tabata, Familial sex-linked mental retardation. *Can Med Assoc J* **87**, 954-956 (1962).

62. R. E. Amir *et al.*, Rett syndrome is caused by mutations in X-linked MECP2, encoding methyl-CpG-binding protein 2. *Nat Genet* **23**, 185-188 (1999).
63. P. Billuart *et al.*, Oligophrenin-1 encodes a rhoGAP protein involved in X-linked mental retardation. *Nature* **392**, 923-926 (1998).
64. G. Neri, C. E. Schwartz, H. A. Lubs, R. E. Stevenson, X-linked intellectual disability update 2017. *Am J Med Genet A* **176**, 1375-1388 (2018).
65. R. E. Stevenson, C. E. Schwartz, R. C. Rogers, Malformations among the X-linked intellectual disability syndromes. *Am J Med Genet A* **161a**, 2741-2749 (2013).
66. R. Guerrini, W. B. Dobyns, Malformations of cortical development: clinical features and genetic causes. *Lancet Neurol* **13**, 710-726 (2014).
67. K. C. Lim, P. B. Crino, Focal malformations of cortical development: new vistas for molecular pathogenesis. *Neuroscience* **252**, 262-276 (2013).
68. Y. Zhang *et al.*, Reduced cortical folding in mental retardation. *AJNR Am J Neuroradiol* **31**, 1063-1067 (2010).
69. G. Juric-Sekhar, R. F. Hevner, Malformations of Cerebral Cortex Development: Molecules and Mechanisms. *Annu Rev Pathol* **14**, 293-318 (2019).
70. J. P. Doyle *et al.*, Application of a translational profiling approach for the comparative analysis of CNS cell types. *Cell* **135**, 749-762 (2008).
71. H. Shangguan *et al.*, Kabuki syndrome: novel pathogenic variants, new phenotypes and review of literature. *Orphanet J Rare Dis* **14**, 255 (2019).
72. M. Wong, The role of glia in epilepsy, intellectual disability, and other neurodevelopmental disorders in tuberous sclerosis complex. *J Neurodev Disord* **11**, 30 (2019).
73. C. Yu *et al.*, White matter tract integrity and intelligence in patients with mental retardation and healthy adults. *Neuroimage* **40**, 1533-1541 (2008).
74. M. D. Spencer *et al.*, Qualitative assessment of brain anomalies in adolescents with mental retardation. *AJNR Am J Neuroradiol* **26**, 2691-2697 (2005).
75. M. M. Paz Soldan, I. Pirko, Biogenesis and significance of central nervous system myelin. *Semin Neurol* **32**, 9-14 (2012).
76. J. George, C. Soares, A. Montersino, J. C. Beique, G. M. Thomas, Palmitoylation of LIM Kinase-1 ensures spine-specific actin polymerization and morphological plasticity. *Elife* **4** (2015).
77. G. M. Elias *et al.*, Synapse-specific and developmentally regulated targeting of AMPA receptors by a family of MAGUK scaffolding proteins. *Neuron* **52**, 307-320 (2006).
78. S. Dutta, P. Sengupta, Men and mice: Relating their ages. *Life Sci* **152**, 244-248 (2016).
79. A. C. Horton, M. D. Ehlers, Dual modes of endoplasmic reticulum-to-Golgi transport in dendrites revealed by live-cell imaging. *J Neurosci* **23**, 6188-6199 (2003).
80. D. Heo *et al.*, Stage-specific control of oligodendrocyte survival and morphogenesis by TDP-43. *Elife* **11** (2022).
81. S. H. Kang, M. Fukaya, J. K. Yang, J. D. Rothstein, D. E. Bergles, NG2+ CNS glial progenitors remain committed to the oligodendrocyte lineage in postnatal life and following neurodegeneration. *Neuron* **68**, 668-681 (2010).
82. M. D. Muzumdar, B. Tasic, K. Miyamichi, L. Li, L. Luo, A global double-fluorescent Cre reporter mouse. *Genesis* **45**, 593-605 (2007).
83. M. V. Sánchez-Gómez, M. P. Serrano, E. Alberdi, F. Pérez-Cerdá, C. Matute, Isolation, Expansion, and Maturation of Oligodendrocyte Lineage Cells Obtained from Rat Neonatal Brain and Optic Nerve. *Methods Mol Biol* **1791**, 95-113 (2018).
84. T. Laux *et al.*, GAP43, MARCKS, and CAP23 modulate PI(4,5)P(2) at plasmalemmal rafts, and regulate cell cortex actin dynamics through a common mechanism. *J Cell Biol* **149**, 1455-1472 (2000).

85. J. Schindelin *et al.*, Fiji: an open-source platform for biological-image analysis. *Nat Methods* **9**, 676-682 (2012).

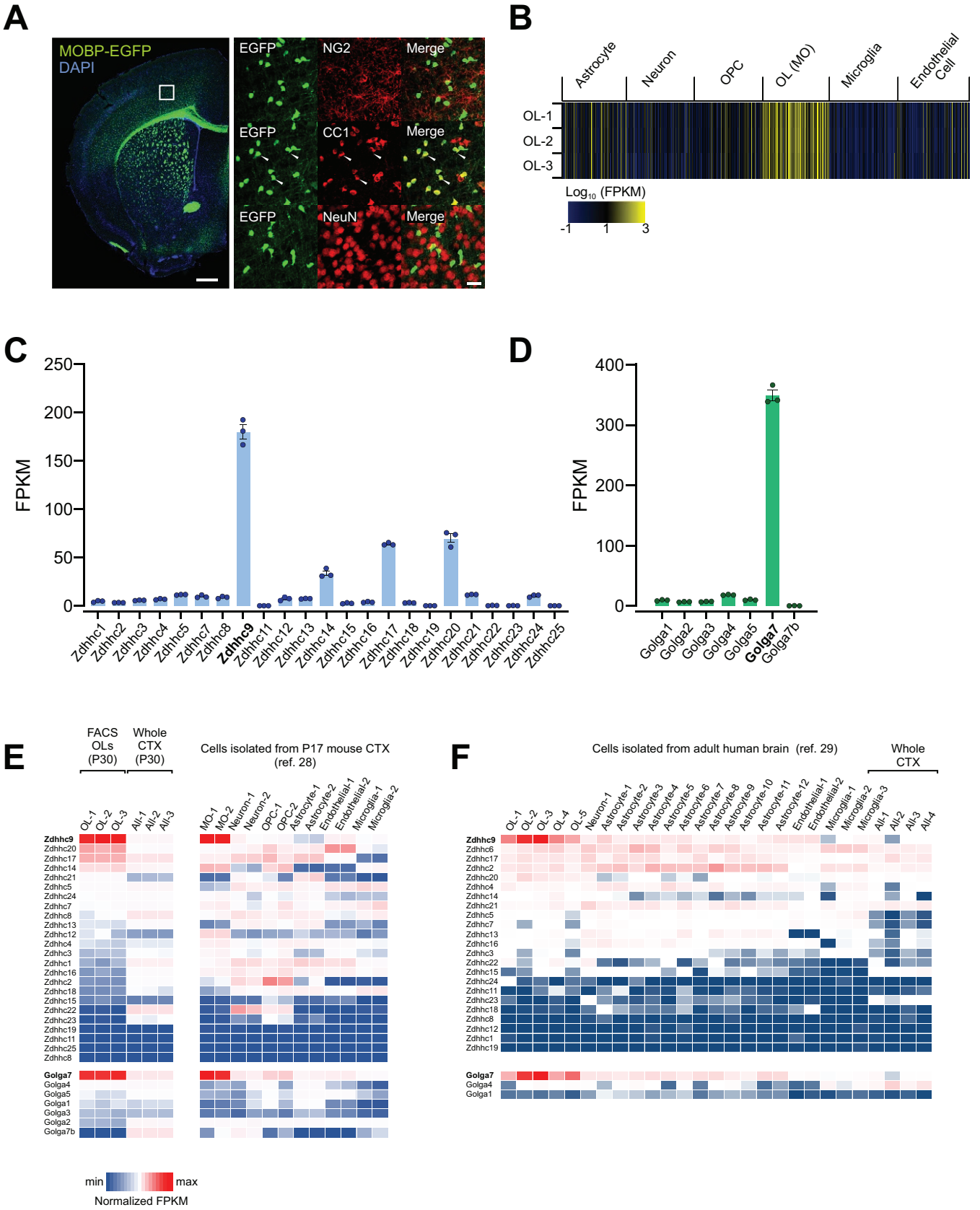

Jeong, Gonzalez-Fernandez et al., Figure 1

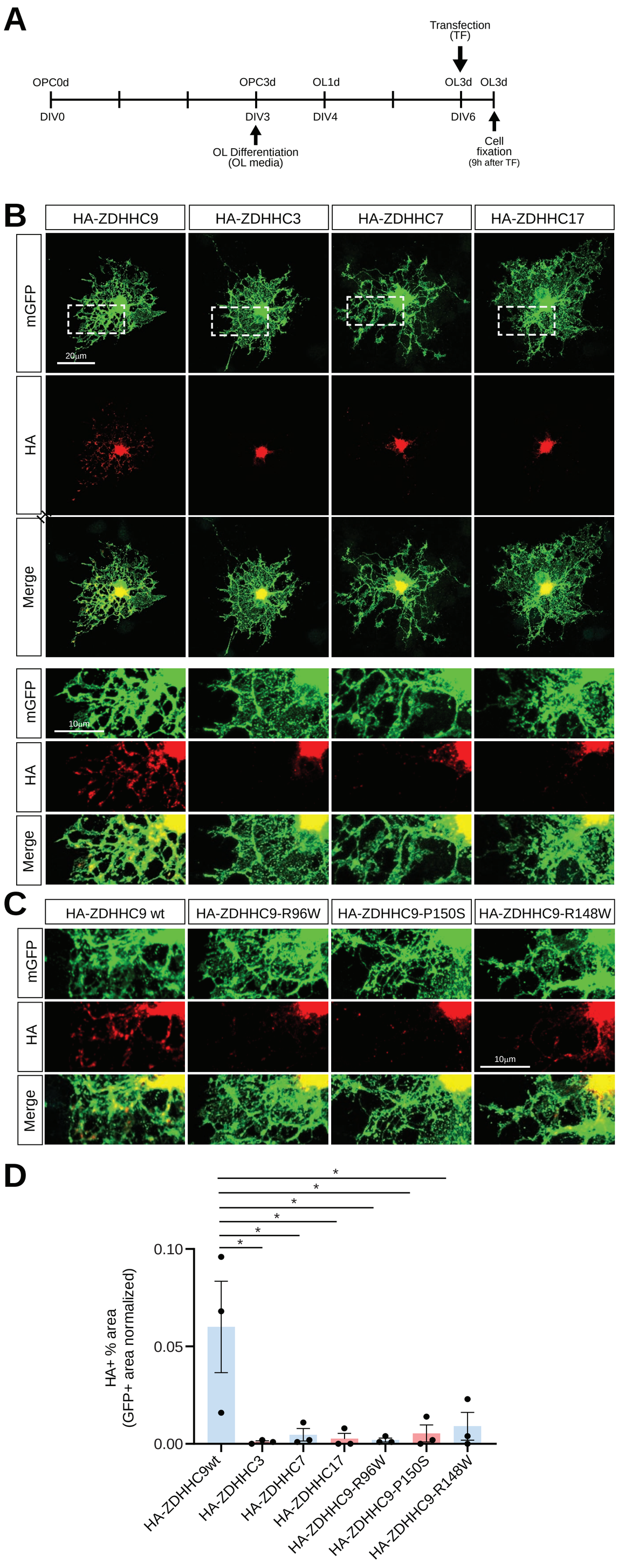

Jeong, Gonzalez-Fernandez et al., Figure 2

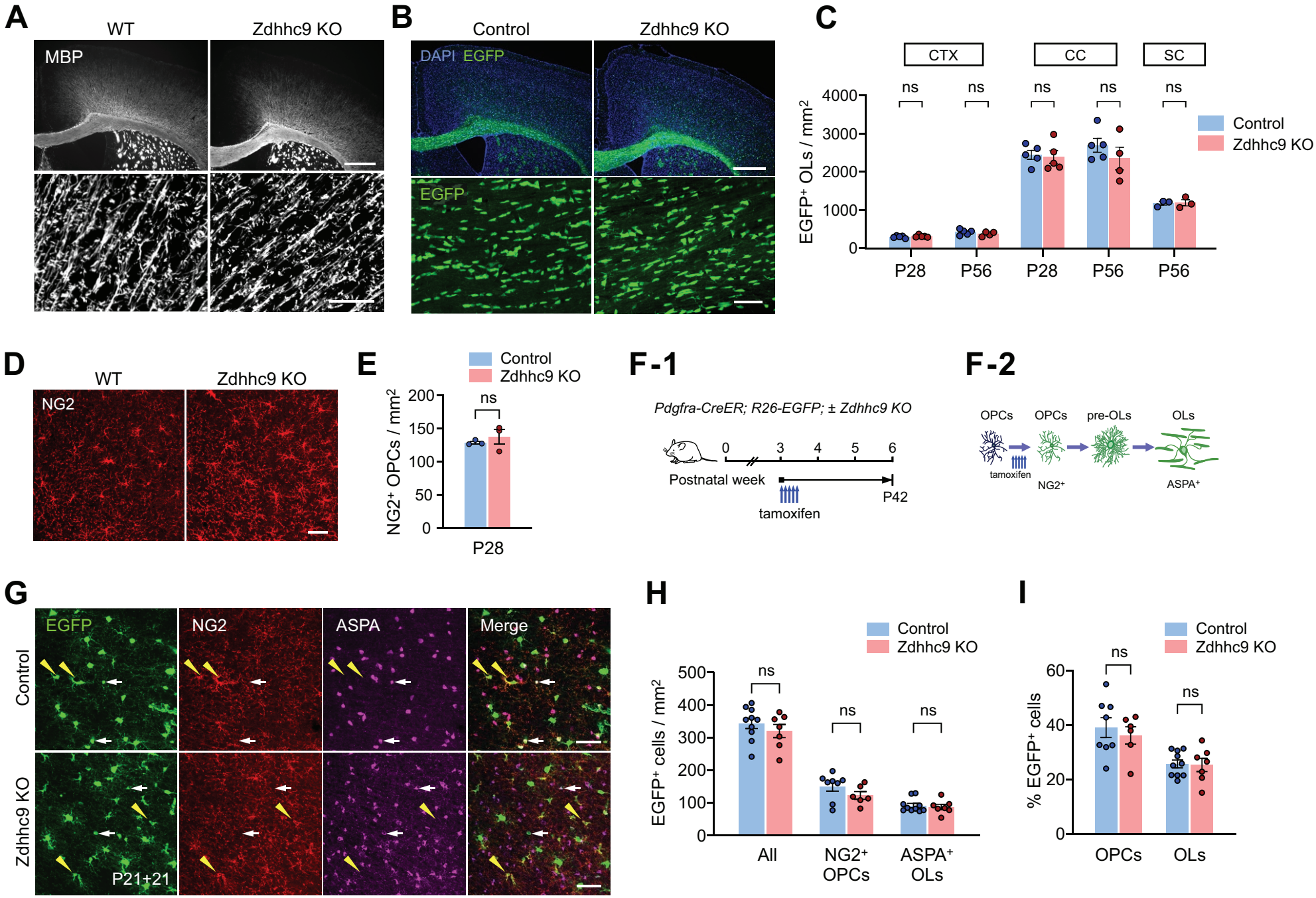

Jeong, Gonzalez-Fernandez et al., Figure 3

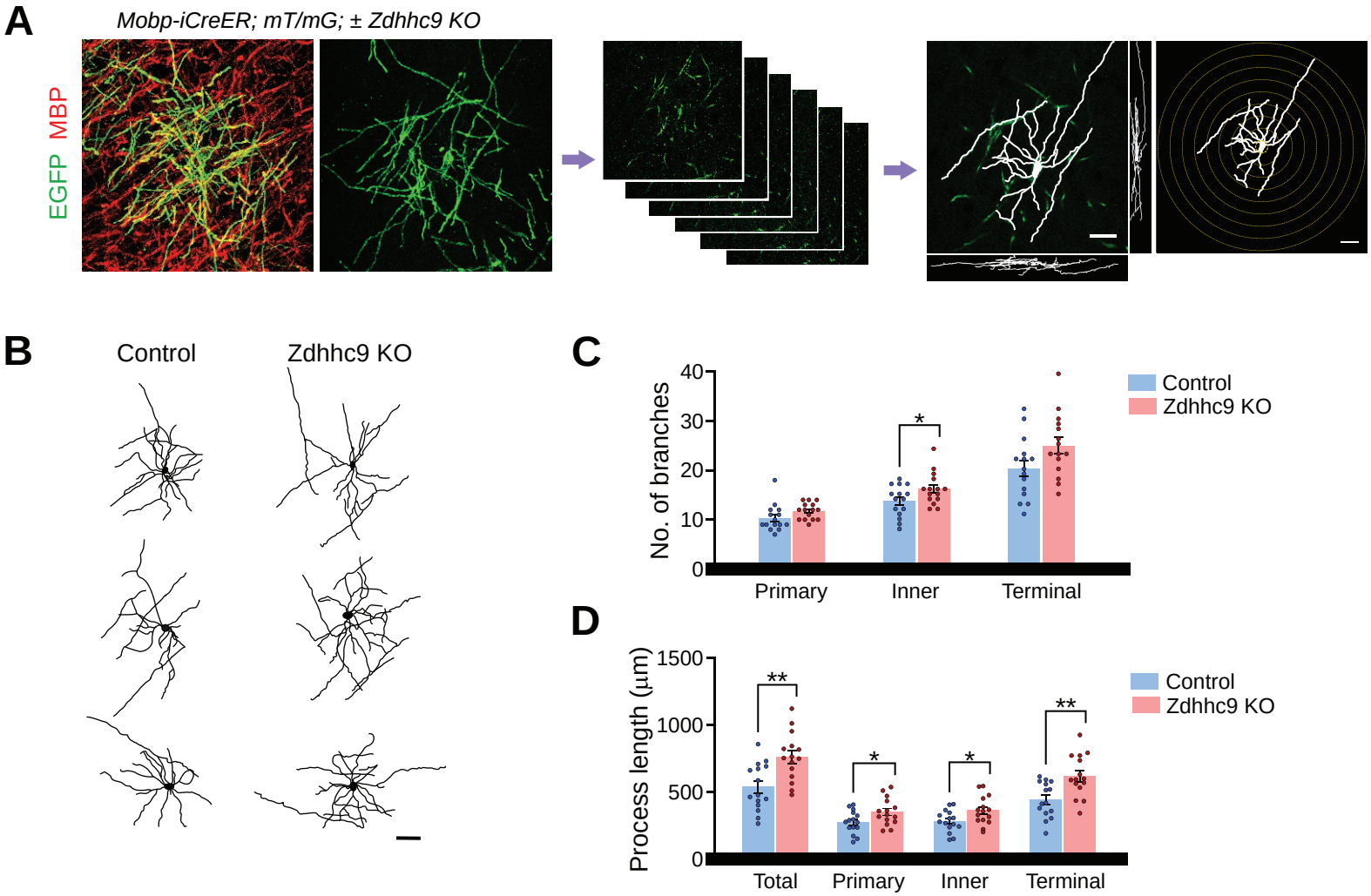

Jeong, Gonzalez-Fernandez et al., Figure 4

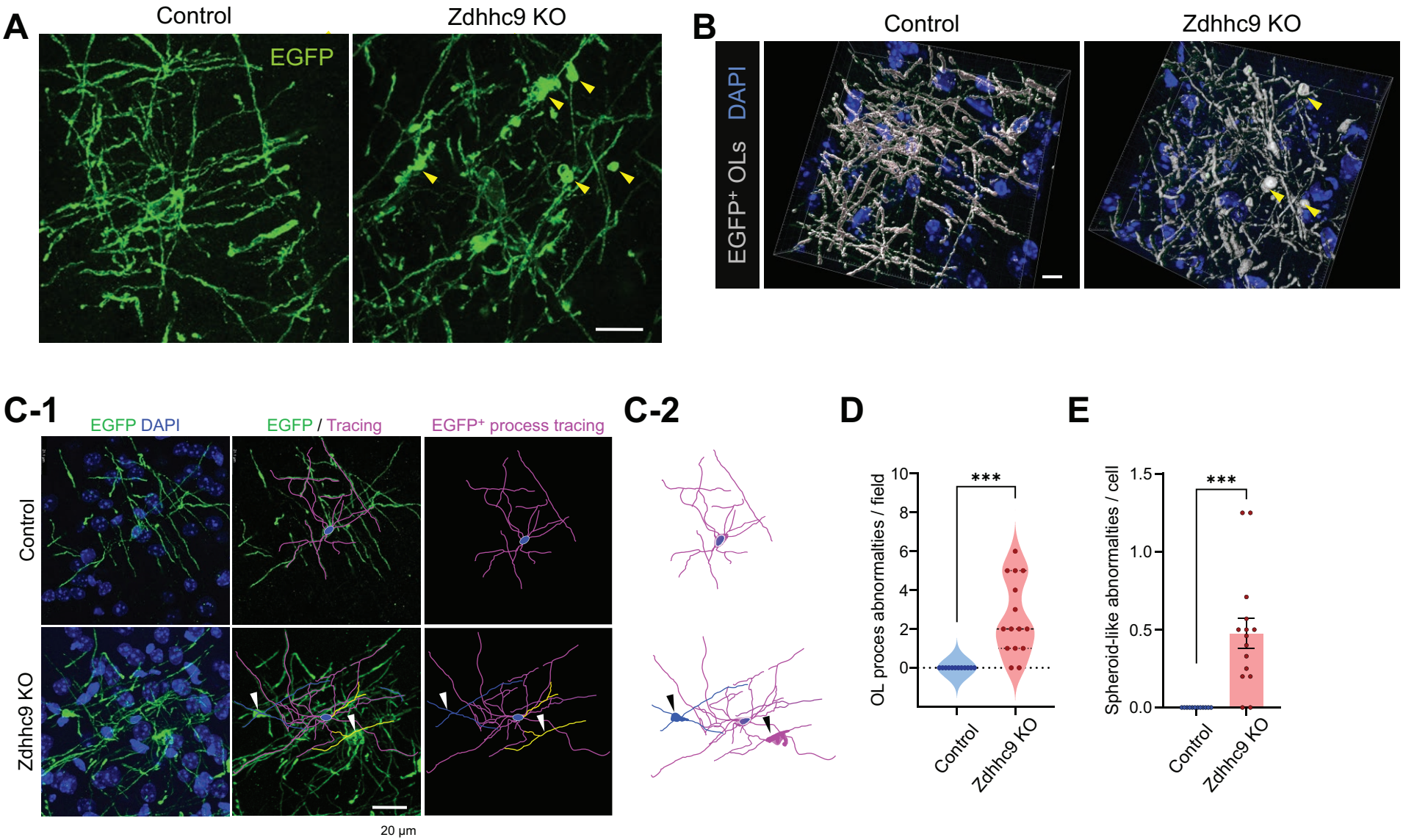

Jeong, Gonzalez-Fernandez et al., Figure 5

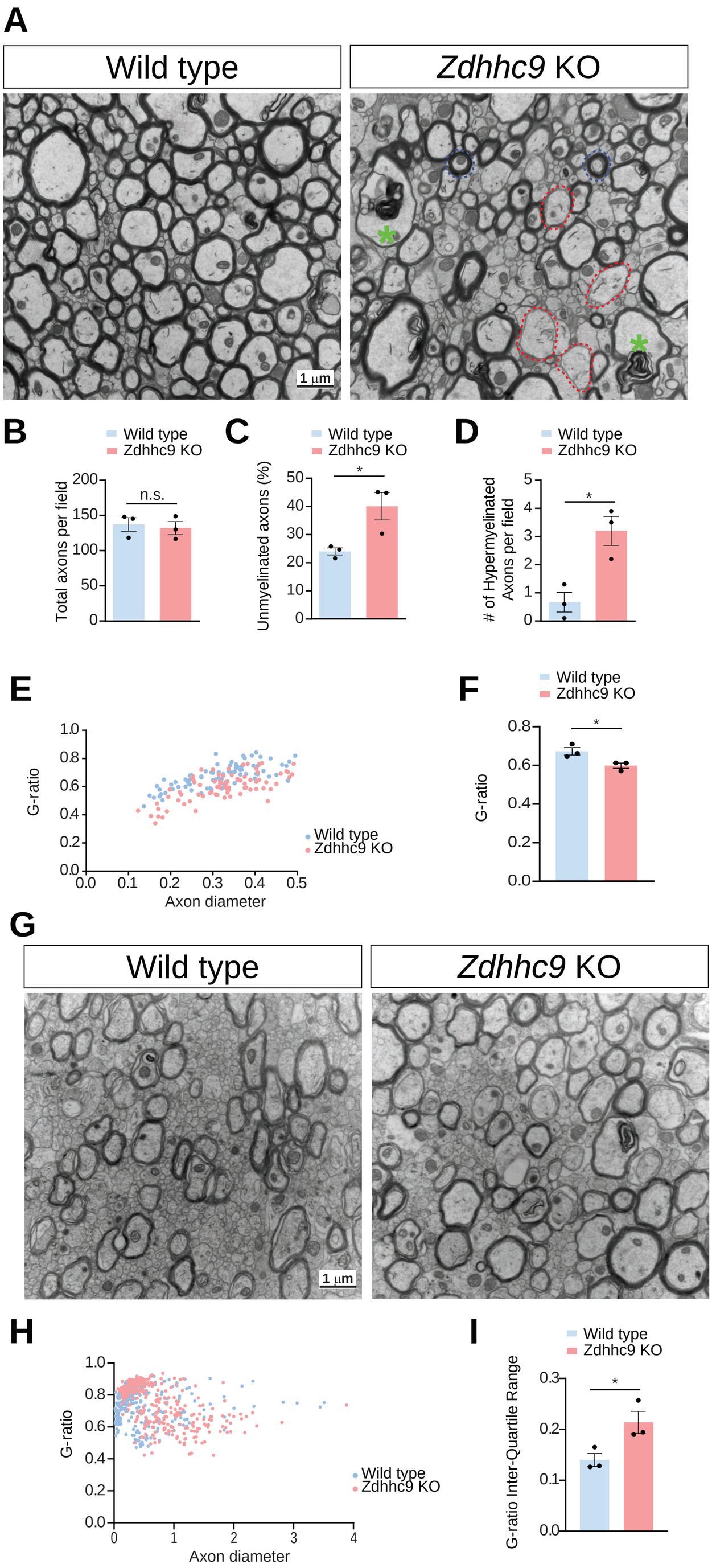

Jeong, Gonzalez-Fernandez et al., Figure 6

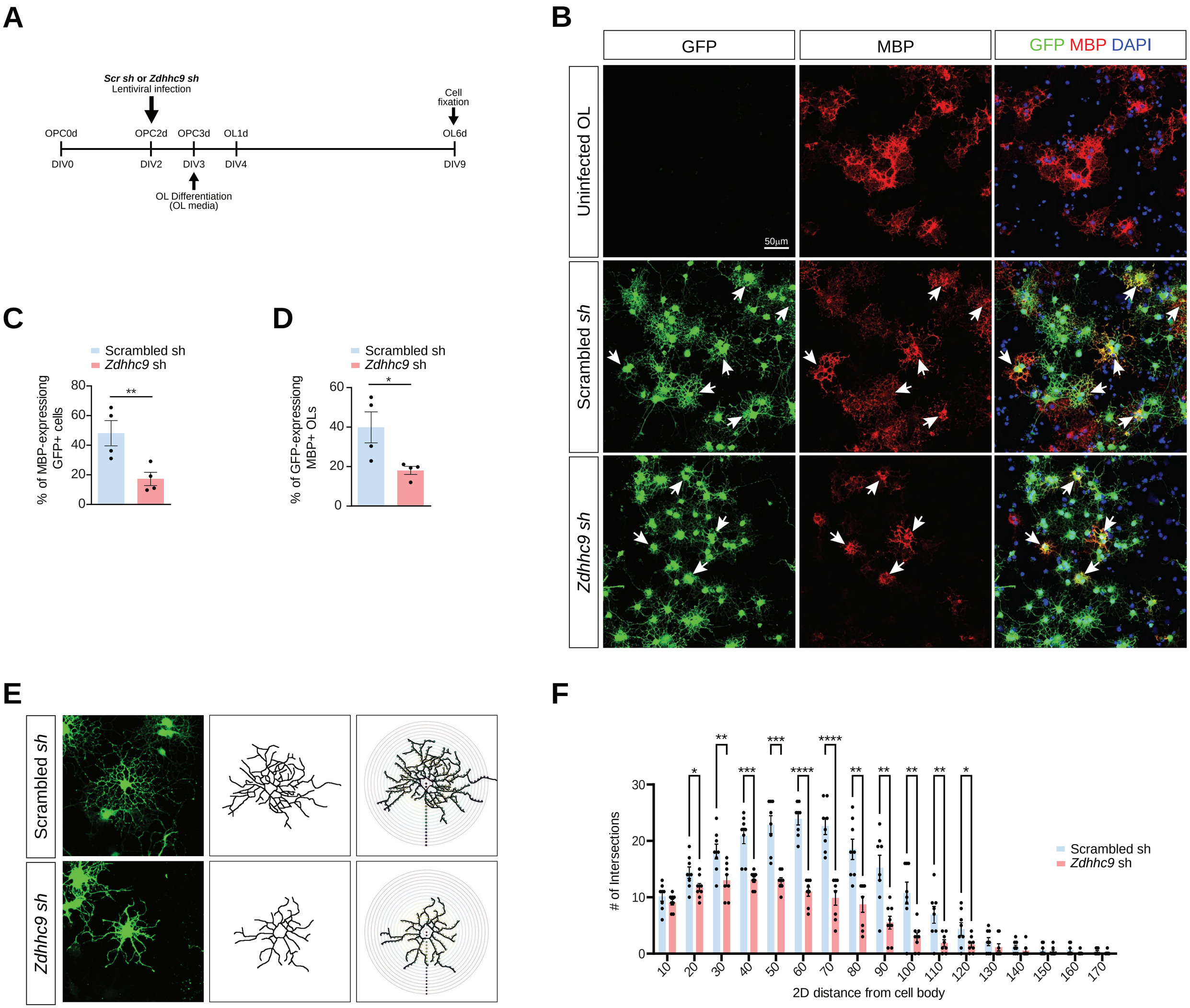

Jeong, Gonzalez-Fernandez et al., Figure 7

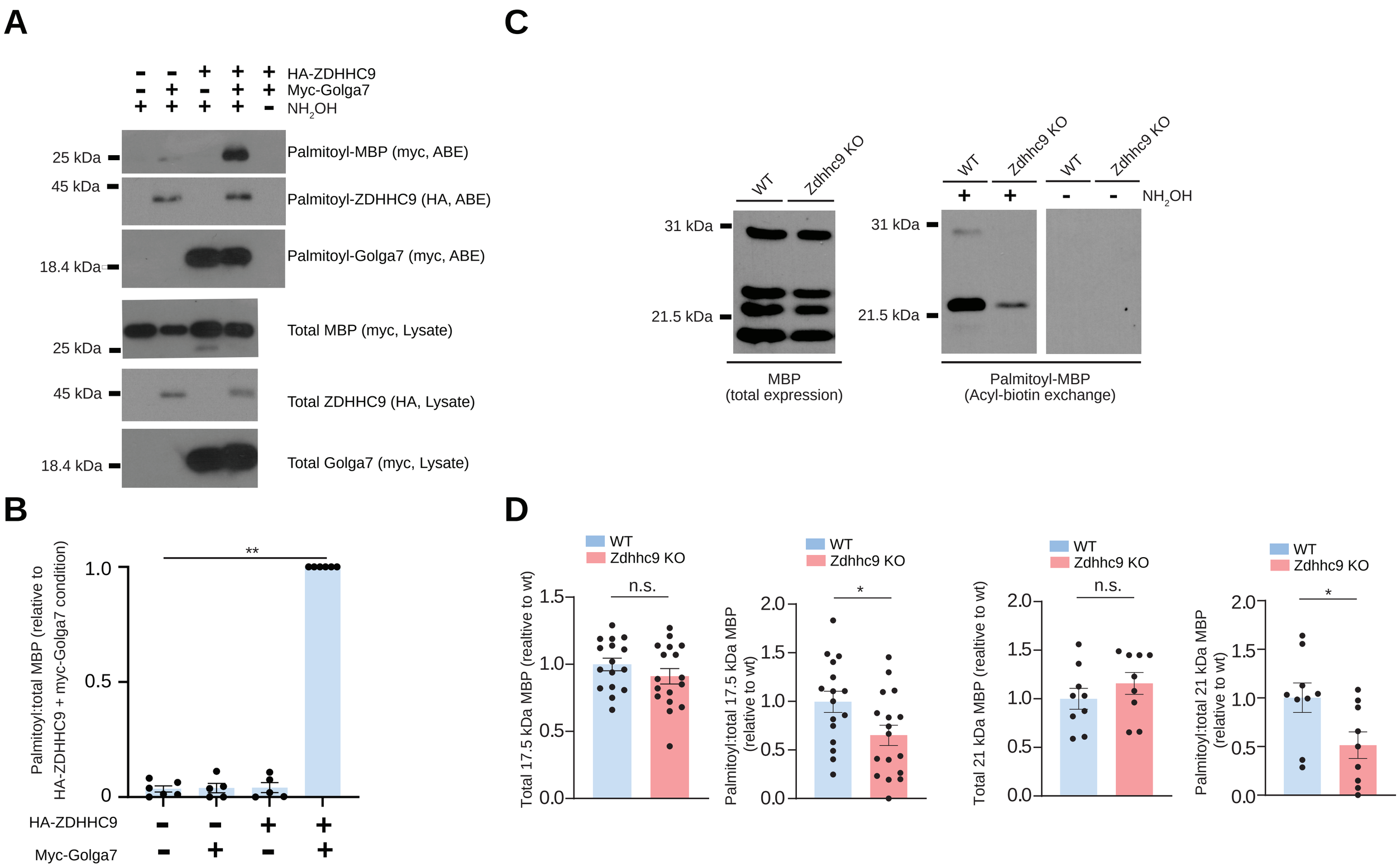

Jeong, Gonzalez-Fernandez et al., Figure 8